

# Accounting for canopy structure improves hyperspectral radiative transfer and sun-induced chlorophyll fluorescence representations in a new generation Earth System model



Renato K. Braghieri <sup>a,b,\*</sup>, Yujie Wang <sup>c</sup>, Russell Doughty <sup>c</sup>, Daniel Sousa <sup>a</sup>, Troy Magney <sup>d</sup>, Jean-Luc Widlowski <sup>e</sup>, Marcos Longo <sup>a</sup>, A. Anthony Bloom <sup>a</sup>, John Worden <sup>a</sup>, Pierre Gentine <sup>f</sup>, Christian Frankenberg <sup>a,c</sup>

<sup>a</sup> Jet Propulsion Laboratory, California Institute of Technology, 4800 Oak Grove Drive, Pasadena, CA 91109, USA

<sup>b</sup> Joint Institute for Regional Earth System Science and Engineering, University of California at Los Angeles, Los Angeles, CA 90095, USA

<sup>c</sup> Division of Geological and Planetary Sciences, California Institute of Technology, Pasadena, CA 91125, USA

<sup>d</sup> Department of Plant Sciences, University of California, Davis, CA, USA

<sup>e</sup> European Commission-DG Joint Research Centre, Institute for Environment and Sustainability, Ispra, VA I-21027, Italy

<sup>f</sup> Department of Earth and Environmental Engineering, Columbia University, New York, NY 10027, USA

## ARTICLE INFO

Editor: Jing M. Chen

### Keywords:

Canopy structure  
Sun-induced chlorophyll fluorescence  
Hyperspectral radiative transfer scheme  
Earth System models  
Energy balance  
Carbon cycle  
NASA orbiting carbon observatory 3

## ABSTRACT

Three-dimensional (3D) vegetation canopy structure plays an important role in the way radiation interacts with the land surface. Accurately representing this process in Earth System models (ESMs) is crucial for the modeling of the global carbon, energy, and water cycles and hence future climate projections. Despite the importance of accounting for 3D canopy structure, the inability to represent such complexity at regional and global scales has impeded a successful implementation into ESMs. An alternative approach is to use an implicit clumping index to account for the horizontal heterogeneity in vegetation canopy representations in ESMs at global scale. This paper evaluates how modeled hyperspectral shortwave radiation partitioning of the terrestrial biosphere, as well as Sun-Induced Chlorophyll Fluorescence (SIF) are impacted when a clumping index parameterization is incorporated in the radiative transfer scheme of a new generation ESM, the Climate Model Alliance (CliMA). An accurate hyperspectral radiative transfer representation within ESMs is critical for accurately using of satellite data to confront, constrain, and improve land model processes. The newly implemented scheme is compared to Monte Carlo calculations for idealized scenes from the Radiation transfer Model Intercomparison for the Project for Intercomparison of Land-Surface Parameterizations (RAMI4PILPS), for open forest canopies both with and without snow on the ground. Results indicate that it is critical to account for canopy structural heterogeneity when calculating hyperspectral radiation transfer. The RMSE in shortwave radiation is reduced for reflectance (25%), absorptance (66%), and transmittance (75%) compared to the scenario without considering clumping. Calculated SIF is validated against satellite remote sensing data with the recently launched NASA Orbiting Carbon Observatory (OCO) 3, showing that including vertical and horizontal canopy structure when deriving SIF can improve model predictions in up to 51% in comparison to the scenario without clumping. By adding a clumping index into the CliMA-Land model, the relationship between canopy structure and SIF, Gross Primary Productivity (GPP), hyperspectral radiative transfer, and viewing geometry at the canopy scale can be explored in detail.

## 1. Introduction

Terrestrial vegetation is the largest carbon sink globally, consistently absorbing almost a third of all anthropogenic carbon emissions

(Friedlingstein et al., 2020). However, the fate of the terrestrial carbon sink in the future is unclear (Friedlingstein et al., 2014; Schimel et al., 2015; Wieder et al., 2015; Arora et al., 2020) and addressing this important uncertainty lies in improving Earth System models (ESMs)

\* Corresponding author at: NASA Jet Propulsion Laboratory, M/S 233-305F, 4800 Oak Grove Drive, Pasadena, CA 91109, USA.  
E-mail address: [renato.k.braghieri@jpl.nasa.gov](mailto:renato.k.braghieri@jpl.nasa.gov) (R.K. Braghieri).

(Sellers, 1997; Prentice et al., 2015; Bonan and Doney, 2018).

Most state-of-the-art land surface models (LSMs) within ESMs are confined to one-dimensional (vertical) radiation transfer, often following a plane-parallel turbid media assumption based on pioneering work from Sellers (1985) and Verhoef (1984). The radiative transfer within vegetation canopies is rather complex because it involves multiple scattering and mutual shadowing of leaves, which are non-infinitesimal elements arranging themselves in hundreds of thousands of different angular configurations.

A number of studies have shown that neglecting 3D vegetation canopy structural features may result in significant biases in estimating the land surface energy and carbon balances. For example, Sprintsin et al. (2012) showed that differences between sunlit and shaded leaves can lead to a significant underestimation of the canopy gross primary productivity (GPP), similar to other studies (Chen et al., 2012; Loew et al., 2014; Braghieri et al., 2019, 2020). In alignment with these previous results, Loew et al. (2014) found that in extreme cases GPP might be underestimated by as much as 25% and surface albedo might be overestimated by up to 36%, leading to a radiative forcing of the order of  $-1.25 \text{ W m}^{-2}$ .

Although highly accurate 3D canopy radiative transfer models have been developed and validated against observations (Wang and Jarvis, 1990a, 1990b; Gastello-Etchegorry, 2008; Duursma and Medlyn, 2012), they often demand extreme computational power and cannot be employed at large scales over long periods of time (Song et al., 2009). Therefore, these highly parameterized 3D radiative transfer models are unsuitable for direct implementation into ESMs. To account for the structural effects of vegetation on radiation partitioning, different parameterizations were developed and applied in radiative transfer models within LSMs, which often work by modulating the optical depth, or the leaf area index (LAI), of the vegetation canopy through the addition of an effective variable, the so-called clumping index (Nilson, 1971; Baldocchi and Harley, 1995; Kucharik et al., 1999; Pinty et al., 2006; Ni-Meister et al., 2010; Braghieri et al., 2019, 2020).

The clumping index characterizes the horizontal spatial distribution of trees and leaves, from small to whole-canopy scales (Nilson, 1971; Norman and Jarvis, 1974), and it can be derived from gap size distribution measured *in-situ* with ceptometers or digital hemispherical photography (DHP) (Chen and Cihlar, 1995; Leblanc et al., 2002; Leblanc et al., 2005; Ryu et al., 2010b; Fang et al., 2018; Yan et al., 2019), as well as from space with multi-angular remote sensing data (Pisek et al., 2015a, 2015b; He et al., 2016) and, more recently, from LiDAR data (Wang and Kumar, 2019).

Although the clumping index has been commonly used to account for the impacts of vegetation structure on radiative transfer modeling and further impacts on land surface processes (Baldocchi et al., 2002; Ryu et al., 2010a; Chen et al., 2012; Braghieri et al., 2019, 2020), previous studies are often limited to broadband spectral analysis in the photosynthetically active radiation (PAR, 400–700 nm) and Near Infrared (NIR, 700–2500 nm), mainly due to the direct applicability of these two broadbands in current ESMs, as well as the limited information about hyperspectral canopy optical properties. However, new generation ESMs should be able to include hyperspectral canopy radiative transfer schemes because high resolution spectral data is now available from aircrafts and will soon be available from space, on the International Space Station (ISS) and later, via the US Surface Biology and Geology (SBG) concept (Schimel and Schneider, 2019; Cawse-Nicholson et al., 2021).

Hyperspectral data can provide a wide range of unique constraints on plant functional traits (Butler et al., 2017). For instance, imaging spectroscopy can map terrestrial vegetation properties, such as canopy water content, leaf nitrogen and phosphorus compositions, as well as a wide range of traits related to photosynthesis, respiration, and decomposition of leaf material (Singh et al., 2015). However, current state-of-the-art ESMs are not able to make use of all the extra information provided by hyperspectral measurements of vegetation, nor are they able to

calculate radiative transfer in such high spectral resolution.

The benefits of using a hyperspectral radiative transfer scheme versus the general broadband spectral analysis used in current LSMs are linked to: (i) the direct inversion of ecosystem related parameters from remotely-sensed data (Dutta et al., 2019; Cheng et al., 2020), that has been broadly used as predictors of ecology related variables, e.g., maximum photosynthetic capacity (Meacham-Hensold et al., 2019), GPP (Dechant et al., 2019), leaf pigments (Féret et al., 2017a, 2017b), plant traits (Féret et al., 2019), and other morphological and physiological properties (Serbin et al., 2014); and, (ii) the reduction of uncertainty in surface albedo (Majasalmi and Bright, 2019), and therefore radiative partitioning and forcing, by moving away from the time-invariant look-up tables of broadband (PAR and NIR) canopy optical properties originally based on a study published more than 30 years ago (Dorman and Sellers, 1989). In addition, biases associated with surface reflectance derivation from remotely-sensed data products are often found when converting hyperspectral radiation to multispectral radiation through convolution across multiple sensors (Burggraaff, 2020).

Previous studies have developed coupled LSMs to simulate Sun-Induced Chlorophyll Fluorescence (SIF) (e.g., the Community Land Model (CLM) 4 (Lee et al., 2015), the Biosphere Energy Transfer Hydrology (BETHY) model (Norton et al., 2019), and the Boreal Ecosystem Productivity Simulator (BEPS) (Qiu et al., 2019)). In studies with CLM and BETHY, the authors coupled the original LSMs, capable of simulating carbon assimilation, ecosystem respiration, as well as the energy and water balances, with the SCOPE (Soil Canopy Observation, Photosynthesis and Energy fluxes) model (van der Tol et al., 2009; Van Der Tol et al., 2014). The SCOPE model is a 1D (vertical) radiative transfer and energy balance model that calculates photosynthesis and chlorophyll fluorescence. SCOPE is based on the 4-stream radiative transfer theory from the SAIL (Scattering by Arbitrarily Inclined Leaves) model (Verhoef, 1984) and the leaf radiative transfer model of Fluspect (Vilfan et al., 2016), which is based upon leaf optical properties from the PROSPECT model (Jacquemoud and Baret, 1990). Apart from recent developments of the SCOPE model to include some representation of canopy vertical heterogeneity (mSCOPE; Yang et al., 2017), a limitation of mSCOPE is that it only accounts for vertical variation in canopy properties, and it has no information about horizontal canopy structure.

While the study with BEPS-SIF (Qiu et al., 2019) has explored the impacts of canopy clumping on SIF emission, the ‘two-leaf’ radiation regime in BEPS (i.e., one vertical vegetation layer with sunlit and shaded leaves) is different from a vertical multi-layered radiative transfer scheme (e.g., two-stream scheme (Sellers, 1985) and 4-stream (Verhoef, 1984)), which had led to divergent impacts of clumping on GPP (Braghieri et al., 2019) and other aspects of the land surface (Bonan et al., 2021).

The main goal of this study is to introduce and evaluate a clumping index parameterization scheme used to represent horizontal vegetation canopy structure within a vertically resolved 1D canopy model, the Climate Model Alliance (CliMA)-Land, within a new generation ESM, the CliMA model. Here, we aim to investigate the impacts of horizontal vegetation canopy structure on hyperspectral shortwave radiation partitioning, as well as to determine if by using a parameterization scheme of vegetation canopy structure through the clumping index, it is possible to make the commonly used SAIL 4-stream theory (Verhoef, 1984) match the shortwave radiation partitioning of a more complex 3D radiative transfer model, raytran (Govaerts and Verstraete, 1995, 1998; Widlowski et al., 2011; Hogan et al., 2018).

Part of the SCOPE model has been incorporated into BETHY but without the inclusion of horizontal canopy heterogeneity. Whereas for the clumping index, several LSMs have used this parameterization scheme in the past (Ni-Meister et al., 2010; Yang et al., 2010; Chen et al., 2012), but without the fully resolved hyperspectral shortwave radiation. Therefore, the main advantage of the clumping index implementation in CliMA-Land is bridging the hyperspectral radiative transfer with explicit consideration of the horizontal canopy heterogeneity. First, the

shortwave radiation partitioning calculated with CliMA-Land is compared with reference values generated in the Radiation transfer Model Intercomparison for the Project for Intercomparison of Land-Surface Parameterizations (RAMI4PILPS) experiment (Widlowski et al., 2011), a radiative transfer model intercomparison exercise. Within the RAMI4PILPS framework, models can be evaluated under perfectly controlled experimental conditions, i.e., all structural, spectral, illumination, and observation related characteristics are known without ambiguity. Therefore, possible deviations between model simulations can thus be directly attributed to the assumptions and shortcuts entering model-specific implementations of the radiative transfer equations. The parameters of a structural parameterization scheme of clumping index (Pinty et al., 2006) are tested in the CliMA-Land hyperspectral radiative transfer model under different scenarios with and without snow.

Second, we use the updated hyperspectral radiative transfer scheme with clumping index to explore the impact of vegetation structure on the estimation of SIF emission (He et al., 2017; Magney et al., 2017; Yang et al., 2019; Zeng et al., 2019; Dechant et al., 2020) and related vegetation indices, commonly used as GPP predictors, such as the fraction of absorbed PAR (fAPAR), absorbed PAR (APAR), and the near-infrared reflectance of vegetation (NIRv) (Badgley et al., 2017; Zeng et al., 2019). We validate the estimation of SIF emission using SIF retrievals from the NASA Orbiting Carbon Observatory 3 (OCO-3) (Eldering et al., 2019) over a subalpine evergreen needleleaf forest in Niwot Ridge, Colorado, and a deciduous broadleaf forest at the University of Michigan Biological (UMB) Station, Michigan, USA. OCO-3's new "snapshot mode" feature enabled by the instrument's ability to swivel and point rapidly, produces measurements over an area of about 80 by 80 km, which allows scanning across a range of view zenith angles over a single overpass within about 2 min. OCO-3 is also unique as far as spaceborne SIF instruments because it samples over the day following the ISS orbit, which also allows a broad coverage of different sun zenith angles.

The rationale behind the SIF evaluation with and without clumping index lies in a number of recent studies suggesting that APAR is among the dominant factors explaining the variability of SIF, and the strong relationship between SIF and GPP (Miao et al., 2018; Wieneke et al., 2018; Yang and van der Tol, 2018; Li et al., 2020; Magney et al., 2020). More recently, a growing number of studies have suggested that APAR alone cannot explain observed SIF variability, and that other factors, such as the physiological SIF emission yield ( $\Phi_p$ ) and the fluorescence escape ratio ( $f_{esc}$ ) would also play a significant role in determining SIF (Du et al., 2017; Migliavacca et al., 2017; Yang et al., 2018; Zeng et al., 2019; Dechant et al., 2020).  $f_{esc}$  has been linked to canopy structure, commonly described in terms of LAI and leaf angular distribution, and more recently to the clumping index (Zeng et al., 2019). In this study we also explore some of the impacts of clumping index on the variability of SIF and its linkage to canopy structural heterogeneity.

## 2. Materials and methods

In this section, firstly, a description of the CliMA-Land radiative transfer model is presented, followed by a description of independent methods of derivation of SIF relationship with other vegetation indices, as well as how canopy structure can impact these relationships. Secondly, a description of the experimental setup and its elements are presented following: (i) a 1D-3D model validation exercise against the RAMI4PILPS dataset (Widlowski et al., 2011), as well as the methodology used to allow a direct intercomparison between broadband and hyperspectral radiative transfer; and (ii) an independent validation against SIF estimates via satellite remote sensed observations over areas of evergreen needleleaf forest and deciduous broadleaf forest with heterogeneous canopy architecture.

### 2.1. CliMA-Land radiative transfer scheme

In this study, we present and evaluate a new important feature of the

canopy radiative transfer model in the land component of a new generation ESM developed by CliMA. The CliMA-Land model addresses soil water movement, plant water transport, stomatal regulation, canopy radiation, and the fluxes of water, carbon, and energy in a highly modular manner. Code and documentation of the in-progress CliMA-Land model are freely and publicly available at <https://github.com/CliMA/Land>.

The CliMA-Land radiative transfer model is based on the vertically heterogeneous mSCOPE (Yang et al., 2017), which uses Fluspect (Vilfan et al., 2016) to simulate leaf reflectance, transmittance, and fluorescence at the leaf level, and SAIL based models to compute spectrally resolved radiative transfer, as well as emitted fluorescence (van der Tol et al., 2016).

The CliMA-Land radiative transfer model was adapted to overcome the assumption of horizontal vegetation homogeneity following a parameterization scheme proposed by Pinty et al. (2006), which accounts for horizontal structural heterogeneity with the addition of an extra parameter, referred to as the clumping index (Nilsson, 1971). Nilsson (1971) first introduced the clumping index ( $\Omega$ ) into the Beer-Lambert's law, to describe plant canopy direct transmittance, or the gap fraction probability ( $P_{gap}(\theta)$ ) as:

$$P_{gap}(\theta) = \exp\left(\frac{-G(\theta) \cdot LAI \cdot \Omega}{\cos\theta}\right) \quad (1)$$

where  $\theta$  is the sun zenith angle, LAI is the leaf area index, and  $G(\theta)$  is the projection coefficient of unit foliage area on a plane perpendicular to the view direction (Ross, 1981).

Analogously to the clumping index, Pinty (2004) developed a parameterization scheme that modulates the canopy optical depth in order to replicate the behavior of more complex 3D radiative transfer schemes but accounting for zenith angular variations of canopy structure. The hypothesis behind this scheme suggests that throughout the day and year, solar radiation crosses different pathways associated with different structures. Therefore, the clumping index also varies with sun zenith angle following:

$$\Omega(\theta) = \zeta(\theta) = -\ln(1 - F_c) \frac{2}{LAI} + b \cdot (1 - \cos\theta) \quad (2)$$

where  $\theta$  is the sun zenith angle, LAI is the leaf area index, and  $F_c$  is the vegetation cover corresponding to the ground fractional cover by all vegetation elements including canopy gaps.

The parameter 'b' has no empirical formulation but it can be derived from observations (Braghieri et al., 2020). Here 'b' is set to zero throughout all the experiments because of its lack of an empirical formulation that would further limit the applicability of CliMA-Land to other sites on Earth where information about clumping zenithal variation is not directly available from remotely-sensed datasets. Therefore, the zenith variation of clumping index is not considered. The clumping index varies with the radiation pathway, which is linked to the viewing zenith angle, but also to the sun zenith angle. The clumping index varying with sun zenith angle can be interpreted as the radiation pathlength varying with sun zenith angle (Kucharik et al., 1999; Pinty et al., 2006; Ryu et al., 2010b). This parameterization scheme was previously implemented, validated, and tested with the land surface model of the UKESM, JULES, following Braghieri (2018), Braghieri et al. (2019, 2020).

The parameterization scheme can be directly implemented into the classical SAIL 4-stream model by assuming that the canopy optical depth is equal to an 'effective LAI' ( $LAI \cdot \Omega$ ) instead of the 'true LAI' (LAI). Hence, the SAIL 4-stream theory can be recast as:

$$\frac{dE_s}{\Omega \cdot LAIdx} = kE_s \quad (3.a)$$

$$\frac{dE^-}{\Omega \cdot LAIdx} = -sE_s + aE^- - \sigma E^+ \quad (3.b)$$

$$\frac{dE^+}{\Omega \cdot LAIdx} = s'E_s + \sigma E^- - aE^+ \quad (3.c)$$

$$\frac{dE_o}{\Omega \cdot LAIdx} = wE_s + \nu E^- + v'E^+ - KE_o \quad (3.d)$$

where  $E_s$  is the direct solar flux,  $E^-$  is the downward diffuse flux,  $E^+$  is the upward diffuse flux, and  $E_o$  is the flux in the viewing direction.  $x$  is the so-called relative optical height, which runs from  $-1$  at the bottom to zero at the canopy top, and LAI.  $k$  and  $K$  are the extinction coefficients dependent on canopy geometrical characteristics, such as the leaf angular distribution, the angular positioning of the sun for  $K$ , and the sun-observer geometry for  $k$ . The remaining scattering coefficients ( $s$ ,  $a$ ,  $\sigma$ ,  $s'$ ,  $w$ ,  $\nu$ ,  $v'$ ) depend on canopy and sun-observer geometry, as well as the canopy optical properties (i.e., leaf reflectance and transmittance). These coefficients were first described in Verhoef (1984) and revisited in Yang et al. (2017).

## 2.2. Determining SIF, $f_{esc}$ , and $NIR_v$

CliMA-Land calculates SIF emission following the mSCOPE model approach (Yang et al., 2017), where the incident radiation is converted into emitted chlorophyll fluorescence on each side of the leaf across all canopy layers and leaf angular orientations. The mSCOPE model framework was used to simulate light scattering within the canopy but using the ‘effective LAI’ ( $LAI \cdot \Omega(\theta)$ ) as the canopy optical depth, instead of ‘true LAI’ (LAI), in order to consider the effects of horizontal canopy heterogeneity on SIF determination via the addition of a clumping index ( $\Omega(\theta)$ ).

The emitted SIF at the top of the canopy in the viewing direction, as well as the hemispherical integration are calculated following the same radiative transfer equations, but also accounting for the emitted radiation. Therefore, SIF estimates depend on the radiative transfer throughout the canopy, the conversion of incident radiation into chlorophyll emission, and finally, the propagation of re-emitted chlorophyll fluorescence through the canopy (van der Tol et al., 2009; Yang et al., 2017).

The far-red part of SIF ( $>740$  nm) is an optical signal in the NIR spectrum in which radiation is highly scattered by leaves allowing only a part of it to escape the vegetation canopy (Knyazikhin et al., 2013; Yang and van der Tol, 2018; Zeng et al., 2019; Dechant et al., 2020). Studies found that reflectance can be used to explain part of the SIF scattering signal (Liu et al., 2016; van der Tol et al., 2016; Badgley et al., 2017; Yang and van der Tol, 2018), but the observed SIF from a tower or from space cannot be totally explained by the cumulative signal of SIF emitted by leaves due to variabilities in canopy structure (Guanter et al., 2014; Zeng et al., 2019; Dechant et al., 2020). Therefore, observed SIF ( $SIF_{obs}$ ) can be described as:

$$SIF_{obs} = APAR \times \Phi_F \times f_{esc} \quad (4)$$

where  $\Phi_F$  is the physiological SIF emission quantum yield of the whole canopy and  $f_{esc}$  is the fluorescence escape ratio, which is a fraction of SIF emitted from leaves that actually escape from the vegetation canopy.

Determining  $f_{esc}$  is rather a difficult task because it requires information about: i) canopy structural properties, such as LAI (Fournier et al., 2012; Yang and van der Tol, 2018), leaf angular distribution (Du et al., 2017; Migliavacca et al., 2017), and the clumping index (Zeng et al., 2019; Dechant et al., 2020); ii) leaf spectral properties; and iii) observation-illumination geometry (Zeng et al., 2019). While a number of studies have explored the influence of  $\Phi_F \times f_{esc}$  together on  $SIF_{obs}$  (Yang et al., 2015; Miao et al., 2018; Wieneke et al., 2018; Li et al., 2020), the potentially strong impact of leaf angular orientation and canopy clumping on  $f_{esc}$  has often been neglected, or overly simplified by treating  $f_{esc}$  as a constant (Guanter et al., 2014). Recently, the whole canopy far-red SIF emission  $f_{esc}$  was approximated by a relationship of

$NIR_v$  and fAPAR following Zeng et al. (2019):

$$f_{esc} \approx \frac{NIR_v}{fAPAR} \quad (5)$$

where  $NIR_v$  is the product of NIR reflectance at 792 nm and NDVI ( $R_{792nm} - R_{687nm}/R_{792nm} + R_{687nm}$ ; Tucker, 1979), a variable that has been shown to be strongly correlated with  $SIF_{obs}$  at large spatiotemporal scales (Badgley et al., 2017). In order to test the impact of clumping index on the validity of Eq. (5), an independent study (Yang and van der Tol, 2018) showed that  $f_{esc}$  can be estimated over a black soil condition as:

$$f_{esc} = \frac{R}{i \times \omega_l} \quad (6)$$

where  $R$  is the NIR reflectance (740 nm),  $i$  is the canopy interceptance, which represents the probability of a photon interacting with the canopy and it is defined as one minus the directional gap fraction (Smolander and Stenberg, 2005),  $\omega_l$  is the leaf single scattering albedo and it corresponds to the fraction of photons at a specific wavelength that escape the canopy (Knyazikhin et al., 2013).

Re-writing Eq. (6) in terms of the escape probability theory (Huang et al., 2007), the recollision probability theory (Smolander and Stenberg, 2005), and the fraction of diffuse radiation,  $f_{esc}$  can be written as:

$$f_{esc} = (1 - f_d) \times \frac{\rho_s}{1 - p_s \times \omega_l} + f_d \times \frac{\rho_d}{1 - p_d \times \omega_l} \quad (7)$$

where  $f_d$  is the fraction of diffuse solar radiation,  $\rho_{s/d}$  is the escape probability of sunlit/shaded leaves,  $p_{s/d}$  is the recollision probability of sunlit/shaded leaves, and  $\omega_l$  is the leaf single scattering albedo. More details on the derivation of Eq. (7) and the equations for  $\rho_{s/d}$  and  $p_{s/d}$  can be found in Appendix A. The impact of clumping index on the relationship described in Eq. (5) is independently tested following the derivation of  $f_{esc}$  through Eq. (7), and fAPAR and  $NIR_v$  directly calculated from CliMA-Land.

In order to verify that the version of CliMA-Land radiative transfer with clumping index is indeed a better approximation of the relationship proposed by Zeng et al. (2019), two popular measures of model parsimony (Aho et al., 2014) were also calculated : the Akaike information criterion (AIC; Akaike, 1973) and the Bayesian information criterion (BIC; Schwarz, 1978). The AIC and BIC are statistical variables used to represent how accurately a determined model fits the data. A better model presents smaller values of AIC and BIC.

## 2.3. RAMI4PILPS benchmarking

Evaluating models can be challenging, especially when it focuses on highly accurate details, such as 3D architectural features of a scene (Kobayashi et al., 2012). There are different ways to evaluate the performance of a specific radiative transfer model including comparisons against different sources of observed data, such as bidirectional reflectance (North, 1996; Malenovský et al., 2008), transmittance (Wang and Jarvis, 1990a, 1990b; Norman and Welles, 1983; Tournebize and Sinoquet, 1995; Law et al., 2001; Sinoquet et al., 2001), and gap fraction measurements (Cescatti, 1997; Kucharik et al., 1999; Yang et al., 2010). The use of these observed datasets is often limited by a restricted spatiotemporal coverage, as well as by a restricted number of suitable instruments. To eliminate uncertainties arising from an incomplete or erroneous knowledge of the structural, spectral, and illumination conditions related to canopy characteristics, typical of model validations with *in-situ* observations, the RADiative transfer Model Intercomparison (RAMI) (Pinty et al., 2001; Pinty, 2004; Widlowski et al., 2007, 2011, 2013, 2015) has been used to evaluate models against the extensively verified 3D reference Monte Carlo model, raytran (Govaerts and Verstraete, 1995, 1998) under perfectly controlled conditions. In particular, the RAMI4PILPS suite of experiments (Widlowski et al., 2011) was

designed to evaluate the accuracy and consistency of shortwave radiative transfer formulations as commonly used in ESMs. Here we use the RAMI4PILPS heterogeneous canopy scenario where tree crowns were approximated by woodless spheres in an open forest canopy scene (see Fig. 1). Details of the RAMI4PILPS experiments used in here are summarized in Table 1. For each scenario, simulations for different LAI values and varying soil albedos are performed, assuming direct radiation for three different sun zenith angles.

We simulate all three components of the radiative partitioning: (i) canopy reflectance, which is defined as the ratio of reflected to incident radiation at the top-of-canopy, (ii) canopy absorption, which is defined as the fraction of radiation entering the canopy through a reference plane at the top-of-canopy, and absorbed by the elements in the scene, and (iii) canopy transmittance, which is defined as the amount of spectral energy transmitted through the vegetation.

#### 2.4. Moving the reference values from two broadbands to hyperspectral resolution

The RAMI4PILPS experiment focused on two separate broadbands (PAR and NIR) to be directly comparable to ESMs, which often make use of the two-stream radiative transfer scheme in these only two broadbands, separately. Therefore, the canopy spectral properties, i.e., leaf reflectance and leaf transmittance, are given as an average value representing the entire broadbands PAR and NIR. In order to move from a broadband radiative transfer scheme to a hyperspectral one, the

**Table 1**

Summary of variables defining structurally heterogeneous scenes (see Widlowski et al. (2011) for details). Different soil albedos are defined as BLK = black, MED = medium, SNW = snow.

Variable Identification	Values (Units)
Leaf Area Index / whole canopy	0.50 <sup>S</sup> , 1.50 <sup>M</sup> and 2.50 <sup>D</sup> ( $\text{m}^2 \cdot \text{m}^{-2}$ )
Leaf Area Index / each tree	5.0 <sup>S</sup> , 5.0 <sup>M</sup> and 5.0 <sup>D</sup> ( $\text{m}^2 \cdot \text{m}^{-2}$ )
1 - P <sub>gap</sub> ( $\theta = 0^\circ$ )	0.09 <sup>S</sup> , 0.26 <sup>M</sup> and 0.43 <sup>D</sup>
Tree density	12.80 <sup>S</sup> , 38.24 <sup>M</sup> and 63.68 <sup>D</sup> (trees/ha)
Maximum canopy height	16 m
Minimum sphere center height	7 m
Maximum sphere center height	11 m
$\alpha_{\text{soil}}$ , PAR / $\alpha_{\text{soil}}$ , NIR	BLK: 0.00/0.00; MED: 0.12/0.21; SNW: 0.96/0.56
Soil scattering law	Lambertian
$\rho_{\text{leaf}}$ , PAR / $\rho_{\text{leaf}}$ , NIR	0.0735/0.3912
$\tau_{\text{leaf}}$ , PAR / $\tau_{\text{leaf}}$ , NIR	0.0566/0.4146
Leaf scattering law	Bi-Lambertian
Sun zenith angle	27.0°/60.0°/83.0°
Scatterer Normal Distribution	spherical
Woody area index	0.0 ( $\text{m}^2 \cdot \text{m}^{-2}$ )

<sup>S</sup> Sparse vegetation condition.

<sup>M</sup> Medium vegetation condition.

<sup>D</sup> Dense vegetation condition.

reference spectral properties were fitted using the Fluspect model (Table 2).

The average broadband values of leaf reflectance PAR ( $\rho_{\text{leaf,PAR}}$ ), leaf

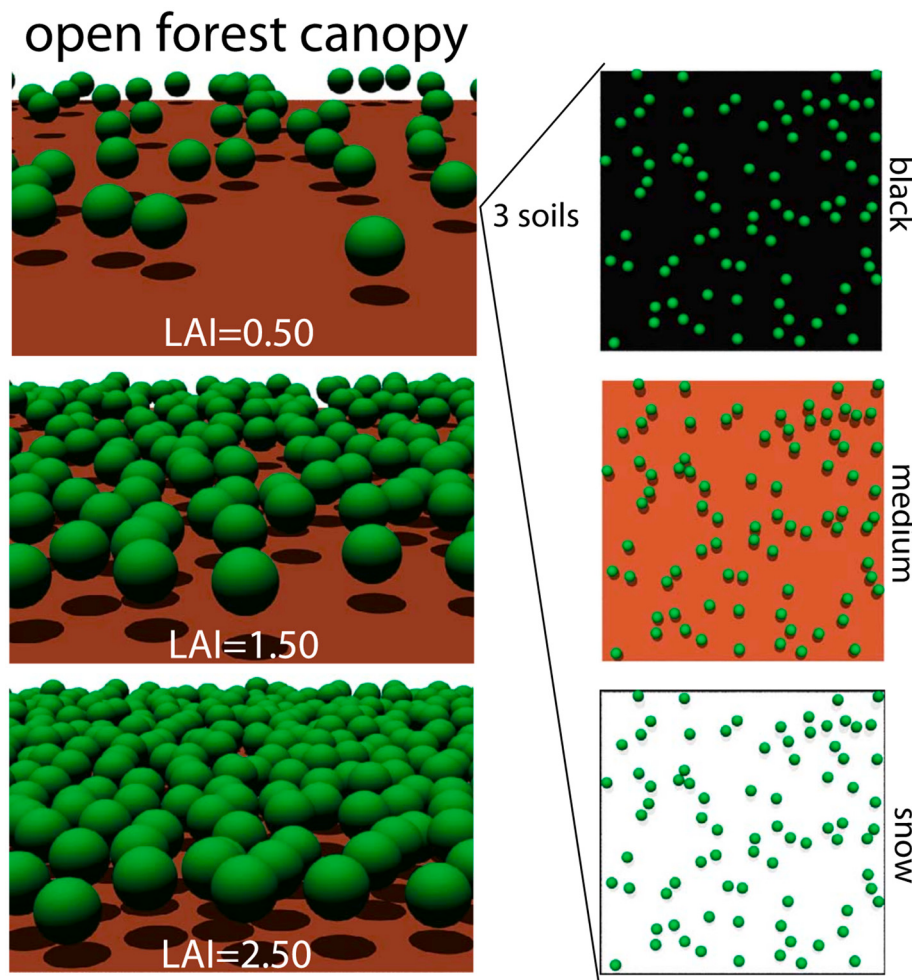


**Fig. 1.** Graphical representation of the open forest canopy environments used in the RAMI4PILPS experiment. Three different leaf area index (LAI) values and three different background soil albedos (adapted from Widlowski et al. (2011)).

**Table 2**

Leaf spectral variables and parameters in leaf biochemical model. See (Féret et al., 2017a; Jacquemoud et al., 2009; Jacquemoud and Baret, 1990) for further details.

Variable	Description	Units	Value
N	Leaf structure parameter	–	1.6
C <sub>ab</sub>	Chlorophyll a + b content	μg cm <sup>-2</sup>	30.0
C <sub>ar</sub>	Carotenoid content	μg cm <sup>-2</sup>	5.0
A <sub>nt</sub>	Anthocyanin content	μg cm <sup>-2</sup>	2.75
C <sub>s</sub>	Senescent material (brown pigments)	fraction	0.0
C <sub>w</sub>	Equivalent water thickness	cm	5.0E-03
C <sub>m</sub>	Dry matter content	μg cm <sup>-2</sup>	0.0
C <sub>x</sub>	Fraction between Zeaxanthin and Violaxanthin in Car (1 = all Zeaxanthin)	fraction	0.0
fqe	Leaf fluorescence efficiency	–	0.01

reflectance NIR ( $\rho_{leaf,NIR}$ ), leaf transmittance PAR ( $\tau_{leaf,PAR}$ ), and leaf transmittance NIR ( $\tau_{leaf,NIR}$ ) were prescribed as  $\rho_{leaf,PAR} = 0.0735$ ,  $\rho_{leaf,NIR} = 0.3912$ ,  $\tau_{leaf,PAR} = 0.0566$ , and  $\tau_{leaf,NIR} = 0.4146$  (Table 1), as previously defined in the RAMI4PILPS experiment. To find the optimal combination of leaf parameters described in Table 2 that approximate the prescribed values of leaf optical properties, each one of the 9 parameters (N, C<sub>ab</sub>, C<sub>ar</sub>, A<sub>nt</sub>, C<sub>s</sub>, C<sub>w</sub>, C<sub>m</sub>, C<sub>x</sub>, and fqe) in its range of plausible values were minimized independently, following the sum of squared difference between modeled and prescribed average  $\rho_{leaf,PAR}$ ,  $\rho_{leaf,NIR}$ ,  $\tau_{leaf,PAR}$ , and  $\tau_{leaf,NIR}$ .

A publicly available customized multiple dimensional optimization algorithm was used to fit leaf spectral parameters (see Data availability). In this method: (i) each parameter in Table 2 is initialized with an initial guess value; (ii) The first parameter (i.e., N) is calculated to minimize the sum of squared error, while holding all the other parameters constant; (iii) this method is repeated for the other variables; (iv) when the set of leaf spectral parameters reaches equilibrium, the increment step decreases in 10%; and (v) steps ii-iv are repeated until all steps were below their solution tolerances ( $10^{-9}$ ).

Nine parameters (Table 2) were fitted to minimize the sum of square difference between modeled and prescribed average  $\rho_{leaf,PAR}$ ,  $\rho_{leaf,NIR}$ ,  $\tau_{leaf,PAR}$ , and  $\tau_{leaf,NIR}$ . To best represent leaf biological properties, we constrained the parameters to their physiological ranges: N in [1,3], C<sub>ab</sub>

in [0,100], C<sub>ar</sub> in [0,30], A<sub>nt</sub> in [0,40], C<sub>s</sub> in [0,1], C<sub>w</sub> in [0,0.05], C<sub>m</sub> in [0,0.5], C<sub>x</sub> in [0,1], and fqe in [0,1].

Fig. 2a shows the hyperspectral canopy reflectance and transmittance minimized against the RAMI4PILPS reference values using Fluspect. The average values for two broadbands separately are shown as circles in Fig. 2b.

## 2.5. Study sites

### 2.5.1. Niwot Ridge, Colorado, USA

The validation study for CliMA-Land radiative transfer simulated SIF was conducted at the subalpine forest of the Niwot Ridge AmeriFlux Core site (US-NR1) in the Rocky Mountains in Colorado, USA (40.03°N, 105.55°W, 3050 m elevation). The forest is composed of three dominant evergreen needleleaf species: lodgepole pine (*P. contorta Douglas ex Loudon*), Engelmann spruce (*Picea engelmannii Parry ex Engelm.*), and subalpine fir (*Abies lasiocarpa (Hook.) Nutt.*). The vegetation canopy structure consists of an average stem density of 4000 stems.ha<sup>-1</sup>, average tree height of 12.5 m, and LAI of 3.8 m<sup>2</sup>.m<sup>-2</sup> (Bowling et al., 2018; Magney et al., 2019). Due to its high elevation, this forest is exposed to cold winters with persistent snowpacks from October to May (Blanken et al., 2009; Burns et al., 2015).

The clumping index at Niwot Ridge was reported as  $0.740 \pm 0.057$  by Sprintsin et al. (2012) after the remote sensing work of Chen et al. (2005) using POLDER (POLARization and Directionality of the Earth's Reflectances; 6 km). However, a more recent algorithm based on MODIS BRDFs (He et al., 2012) reports a clumping index of 0.48 for the 500 m pixel that includes the US-NR1 flux tower. The main difference from the MODIS clumping index and the one from POLDER is the spatial resolution.

### 2.5.2. UMB Station, Michigan, USA

The validation study for CliMA-Land radiative transfer simulated SIF was conducted at a maturing aspen-dominated forest AmeriFlux Core site (US-UMB) in the upper Great Lakes region in Michigan, USA (45.58°N, 84.72°W, 234 m elevation). The forest is composed of dominant deciduous broadleaf species: bigtooth aspen (*Populus grandidentata*) and trembling aspen (*Populus tremuloides*), but with significant presence of maple (*Acer rubra*, *A. saccharum*), red oak (*Quercus rubra*), birch

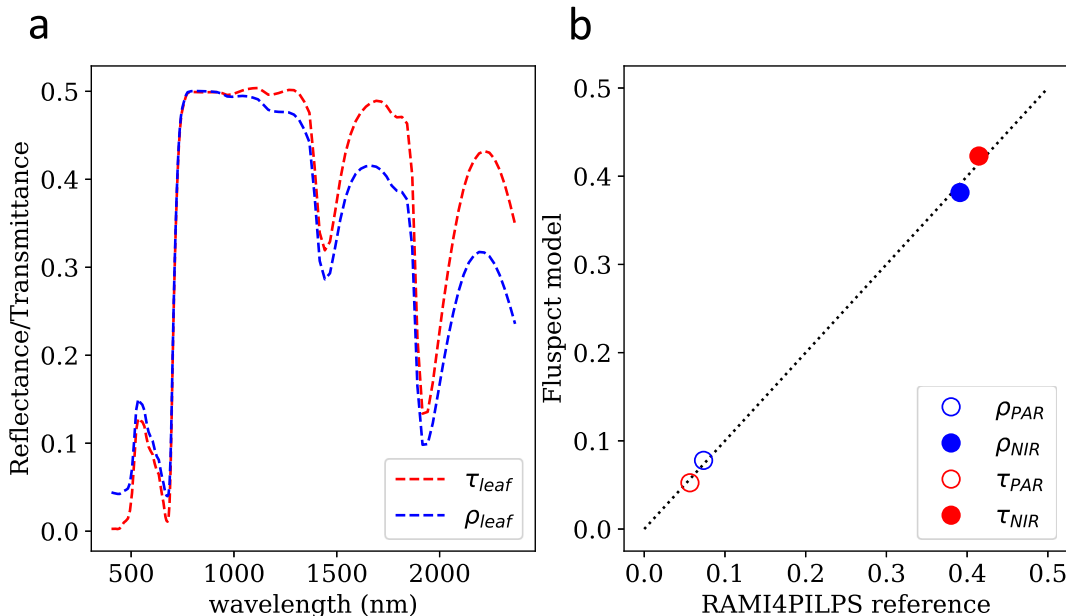


**Fig. 2.** a. Hyperspectral leaf reflectance (blue) and leaf transmittance (red) obtained from Fluspect using values given in Table 2; b. The average values of these curves are represented by circles for two broadbands and single scattering albedo term, separately, i.e., PAR (400–700 nm) and NIR (700–2500 nm); reflectance ( $\rho$ ) and transmittance ( $\tau$ ).

(*Betula papyrifera*), and beech (*Fagus gran-difolia*) as well. The vegetation canopy structure consists of an average stem density of 700–800 stems.  $\text{ha}^{-1}$ , average tree height of ~22 m, and LAI of  $3.5 \text{ m}^2 \cdot \text{m}^{-2}$  (Schmid, 2003; Gough et al., 2013). The clumping index at UMB was reported as  $0.700 \pm 0.047$  by Sprintsin et al. (2012) after the remote sensing work of Chen et al. (2005) and 0.52 from MODIS BRDFs for the 500 m pixel that includes the US-UMB flux tower.

## 2.6. OCO-3 SIF retrievals

To assess the effect of the clumping index on CliMA-Land radiative

transfer model estimates of SIF, we compared simulated SIF computed with and without the clumping index to spaceborne SIF retrievals from the NASA's Orbiting Carbon Observatory 3 (OCO-3). We ran the model for each OCO-3 sounding in three snapshot area maps (SAMs) taken by OCO-3 at Niwot Ridge, Colorado, USA, two of which were obtained on June 12th and June 16th, 2020, and two SAMs at UMB Station, Michigan, USA, taken on August 6th and August 11th, 2020.

OCO-3 is a spectrometer that is similar to OCO-2 and is on the ISS. OCO-3 has the unique ability to obtain SAMs by scanning a target several times in a single overpass with scans being offset to obtain a wider sampling of the Earth's surface, which yield large contiguous

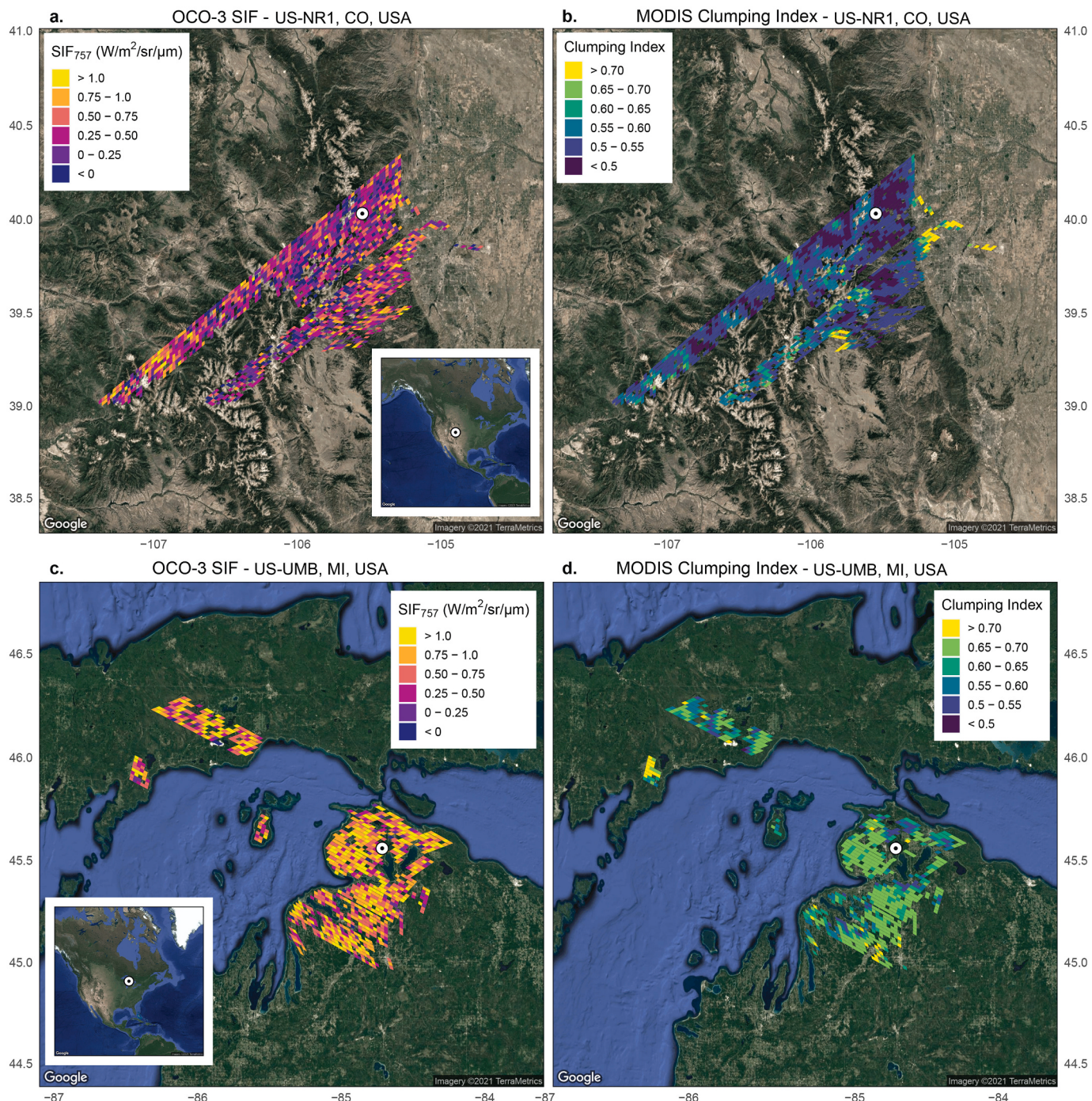


**Fig. 3.** OCO-3 retrieved SIF at 757 nm over a. Niwot Ridge, Colorado, USA on June, 12th, 2020, and c. UMB Station, Michigan, USA on August 11th, 2020. MODIS derived clumping index map from He et al. (2012) over b. Niwot Ridge, Colorado, USA and d. UMB Station, Michigan, USA, for the year of 2006 matching the OCO-3 scan. The white circle with a black dot in the middle represents the position of the flux towers for reference.

scans of  $\sim 100$  km by 100 km (Eldering et al., 2019). The spatial resolution of each OCO-3 sounding footprint is  $\leq 4$  km, with the size varying due to viewing geometry. The ISS orbit is precessing rather than sun-synchronous and it orbits the Earth about 16 times a day, thus overpasses do not occur at the same local time for any latitude and the amount of time between overpasses for any given target location is highly variable and unpredictable in the long term.

For each sounding footprint, the OCO-3 data provides, among other variables, solar and viewing zenith and azimuth angles, instantaneous SIF retrieved at 757 nm ( $SIF_{757}$ ), landcover classification, cloud flags, and quality control flags (Frankenberg et al., 2014; Taylor et al., 2020). From these sun and sensor geometries, we calculated relative azimuth and phase angles for each sounding. Prior to analysis, we removed soundings classified as barren or urban and also those soundings not classified as 'best' by the quality control flag and 'clear' by the cloud flag.

We also calculated area weighted mean LAI,  $C_{ab}$ , and clumping index for each sounding. We have illustrated  $SIF_{757}$  and the clumping index for one of the June 12th, 2020 overpasses in Fig. 3. The LAI map, PROBA-V LAI V2, was produced by Copernicus at 1 km resolution (Fuster et al., 2020) without consideration of any canopy, understory, or foliage clumping effects, as stated in their Algorithm Theoretical Basis Documents (ATBD) (Verger et al., 2019). The temporal resolution is variable, but the file we used had a start date of January 3rd, 2020 and an end date of June 30th, 2020. The  $C_{ab}$  map had a spatial resolution of 0.5 degrees and a weekly temporal resolution for the years 2003–2011 (Croft et al., 2020). To approximate differences in  $C_{ab}$  between pixels during the OCO-3 overpass, we computed weekly means using all years and used  $C_{ab}$  concentrations from the week in which the overpasses occurred (weeks 24 and 25).

The global MODIS-derived clumping index map produced by He et al. (2012) was used to provide a clumping index estimate for the CliMA-Land radiative transfer model. The global clumping index map has a spatial resolution of 500 m and was produced for the year of 2006. We assume that the global clumping index map derived for 2006 data is reliable for usage in 2020 since the interannual variability of clumping index is generally small (He et al., 2016). The data were derived from the NASA-MODIS BRDF/albedo product (MCD43) by considering the difference in forward and backward scattering from the surface, which is primarily controlled by the structure of the vegetation (Braghieri et al., 2019). The MODIS clumping index (He et al., 2012) is an average for all view zenith angles, not specific to nadir or other angles. It can be derived from different combinations of hotspot and dark spot values, but the authors used nadir for hotspot and  $47.7^\circ$  for dark spot in order to produce a map that correlates well with observed *in-situ* measurements.

After simulating instantaneous  $SIF_{757}$  for each OCO-3 sounding using the CliMA-Land radiative transfer model and input data from OCO-3 sun-sensor geometries and area weighted mean LAI,  $C_{ab}$ , and clumping index, we grouped soundings by phase angle and computed the mean for each group. Individual SIF retrievals are noisy and differences in sun-sensor geometry between soundings can contribute to differences in the retrieved SIF values. Thus, it is advised not to use individual soundings for analysis, but retrievals can be averaged across space and/or time to reduce their standard errors and offset potential differences in viewing geometry (Frankenberg et al., 2014; Köhler et al., 2018; Doughty et al., 2019). Thus, the points in Fig. 3 are mean  $SIF_{757}$  values of soundings from a single orbit with nearly identical viewing geometries and the error bars represent the standard error of the mean for that group of soundings. Groups with fewer than 10 soundings ( $n < 10$ ) were excluded from the analysis. We ran the model for each OCO-3 sounding footprint, not only for the sounding including the flux tower (represented by a white circle with a black dot in the middle in Fig. 3 for reference). To reduce the error, we take their means where sun-sensor geometry is nearly identical.

Topographic effects can be observed on OCO-3 CO<sub>2</sub> retrievals due to air mass dependencies, but no effect on retrieved SIF. It appears the main

effect is physiological in a direct comparison of OCO-2 targets and CFIS (airborne) overpasses to tower SIF at Niwot Ridge (Parazoo et al., 2019).

### 3. Results

#### 3.1. Validating canopy radiative partitioning: broadbands PAR and NIR

Fig. 4a shows the three components of the radiation partitioning (lines) using the default case (no clumping) and the respective RAMI4PILPS reference values (circles) for the sparse canopy case with LAI = 0.5 m<sup>2</sup>.m<sup>-2</sup> and  $\sim 10\%$  vegetation cover over a black soil ( $\alpha_{soil} = 0.0$ ). Fig. 4b shows the same example but including clumping derived from Eq. (2), with  $\Omega = 0.37$  and  $b = 0.0$ . For similar figures for all the other canopy structures and soil albedos, see Supplemental material.

Fig. 5 shows a total of 27 cases (3 canopy densities, 3 soil albedos, and 3 sun zenith angles) for two separate wavebands (PAR and NIR) evaluated separately for reflectance, absorptance, and transmittance. For the PAR and NIR wavebands, the addition of canopy clumping improved the agreement between CliMA-Land and the RAMI4PILPS reference values for all terms of the radiation partitioning.

In the PAR waveband, accounting for clumping index significantly improves the model predictive skill, as RMSE dropped from 0.12 to 0.03 for reflectance, from 0.21 to 0.06 for absorptance, and from 0.22 to 0.06 for transmittance. The addition of clumping improved the  $r^2$  for all terms of the radiative partitioning to  $r^2 > 0.97$ . The 1D case underestimates reflectance and transmittance, while overestimates absorptance over all the evaluated cases.

In the NIR spectral region, the addition of clumping significantly improves the  $r^2$  for all terms of the radiative partitioning: from  $r^2 = 0.87$  to  $r^2 = 0.98$  for reflectance; from  $r^2 = 0.73$  to  $r^2 = 0.97$  for absorptance, and for transmittance from  $r^2 = 0.90$  to  $r^2 = 0.99$ . The clumping index parameterization scheme has decreased the RMSE for reflectance (from RMSE = 0.05 to RMSE = 0.02), for absorptance (from RMSE = 0.13 to RMSE = 0.04), and for transmittance (from RMSE = 0.17 to RMSE = 0.08).

These results indicate that the addition of clumping improves the agreement between the 1D and the 3D cases for all terms of the radiation partitioning for both spectral regions.

#### 3.2. Validating canopy radiative partitioning: hyperspectral shortwave radiation

The three hyperspectral components of the radiation partitioning were compared to the RAMI4PILPS reference values. Fig. 6 shows one example of the three components of the hyperspectral radiation partitioning (lines) using the default case (no clumping) and the modified version with clumping. The average values for PAR and NIR are shown as circles and the respective RAMI4PILPS reference values are shown as crosses. Fig. 6 shows the sparse canopy case with LAI = 0.5 m<sup>2</sup>.m<sup>-2</sup> and  $\sim 10\%$  vegetation cover over a black soil ( $\alpha_{soil} = 0.0$ ) for a sun zenith angle of  $27^\circ$ . For similar figures for all the other canopy structures and zenith angles, see Supplemental material. The hyperspectral cases were only evaluated over a black soil albedo due to complexities involved in scaling up soil albedos in the presence of snow. Polar plots showing the difference in far-red SIF, NDVI, and NIRv between the clumped and non-clumped cases can be found in Supplemental material.

Fig. 7 shows a total of 18 cases (3 canopy densities, 3 sun zenith angles, and two spectral regions) for reflectance, absorptance, and transmittance. The addition of canopy clumping improved the agreement between CliMA-Land and the RAMI4PILPS reference values for all terms of the radiation partitioning.

For reflectance, the RMSE between CliMA-Land and the RAMI4PILPS reference values dropped from 0.04 to 0.03 when clumping was considered. For absorptance, the RMSE between CliMA-Land and the RAMI4PILPS reference values dropped from 0.17 to 0.05 when clumping was considered. For transmittance, the RMSE between CliMA-Land and

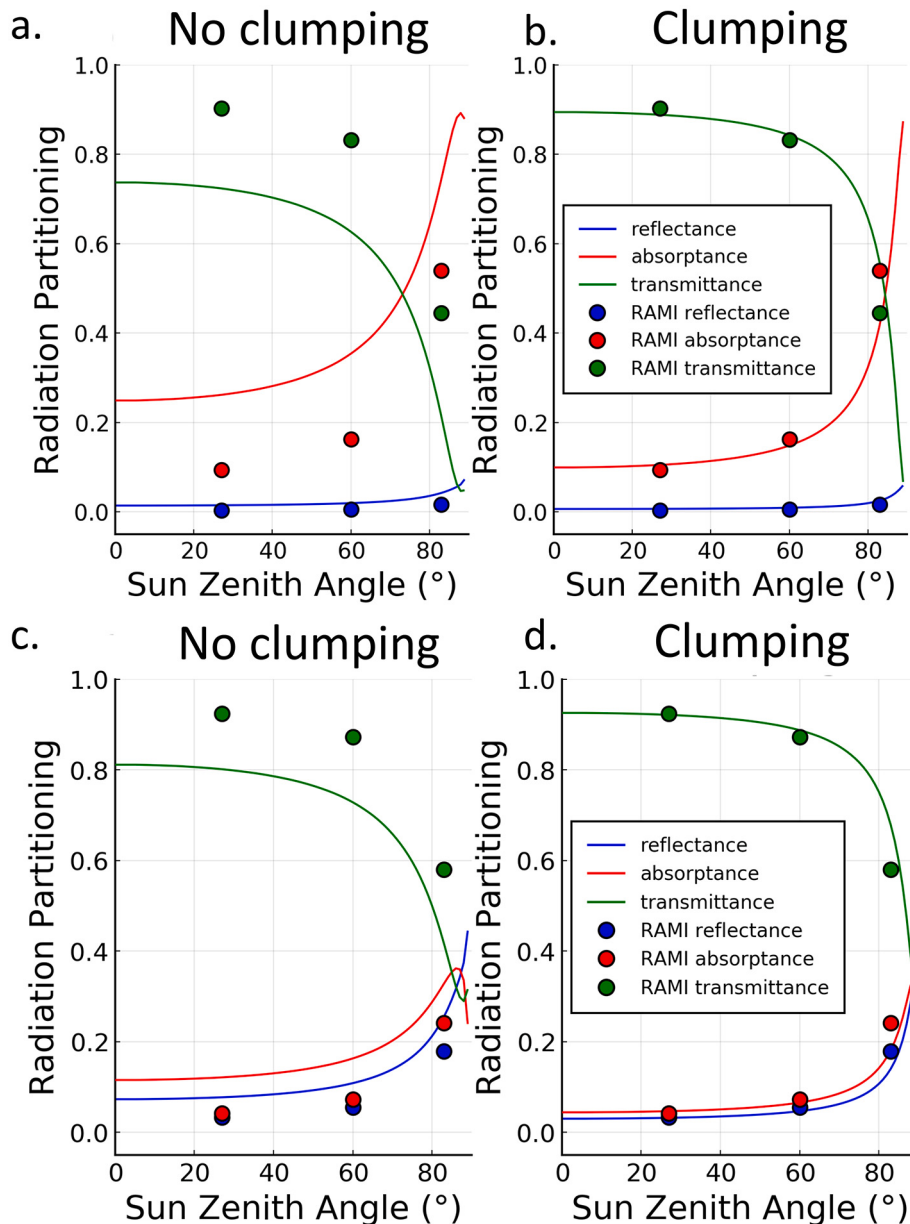


**Fig. 4.** Intercomparison of zenith profile of the fraction of direct absorbed (red), reflected (blue), and transmitted (green) (a–b) PAR (400–700 nm) and (c–d) NIR (700–2500 nm) calculated with 2 different model setups with (clumping) and without clumping (no clumping), and the RAMI4PILPS reference values obtained with a 3D Monte Carlo ray-tracing model, raytran.

the RAMI4PILPS reference values dropped from 0.20 to 0.06 when clumping was considered. The 1D case overestimates reflectance and absorptance, while underestimates transmittance over all the evaluated cases. The addition of clumping has also improved the  $r^2$  for all terms of the radiative partitioning (from  $r^2 = 0.98$  to  $r^2 = 0.99$  for reflectance; from  $r^2 = 0.86$  to  $r^2 = 0.98$  for absorptance; and from  $r^2 = 0.89$  to  $r^2 = 0.97$  for transmittance). These results indicate that clumping has improved the agreement between the 1D and the 3D cases throughout all wavelengths in the shortwave radiation spectrum from 400 to 2500 nm.

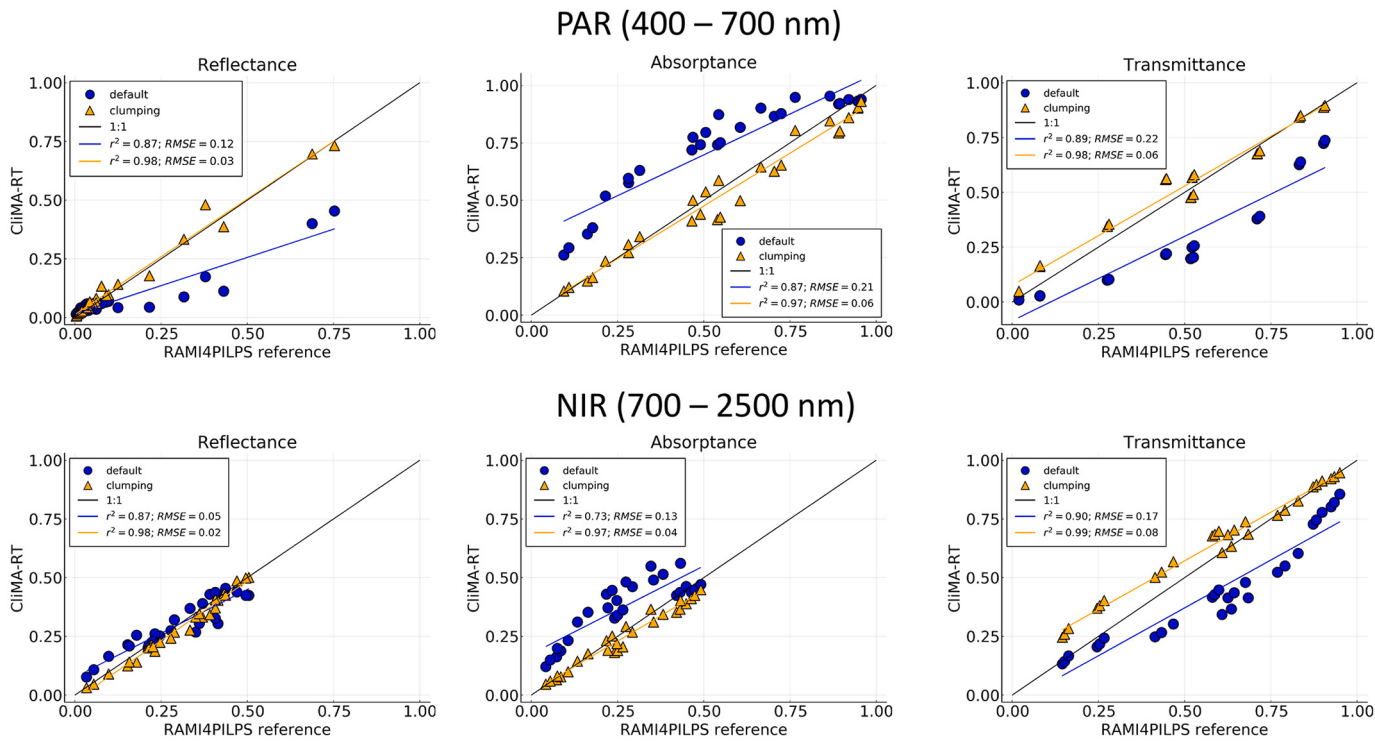
### 3.3. Validating SIF emission with OCO-3 observations

In order to estimate the effect of the clumping index on model estimates of SIF from CliMA-Land radiative transfer, we also compared simulated SIF computed with and without the clumping index to canopy-scale remote sensing SIF retrievals from OCO-3 on board of the

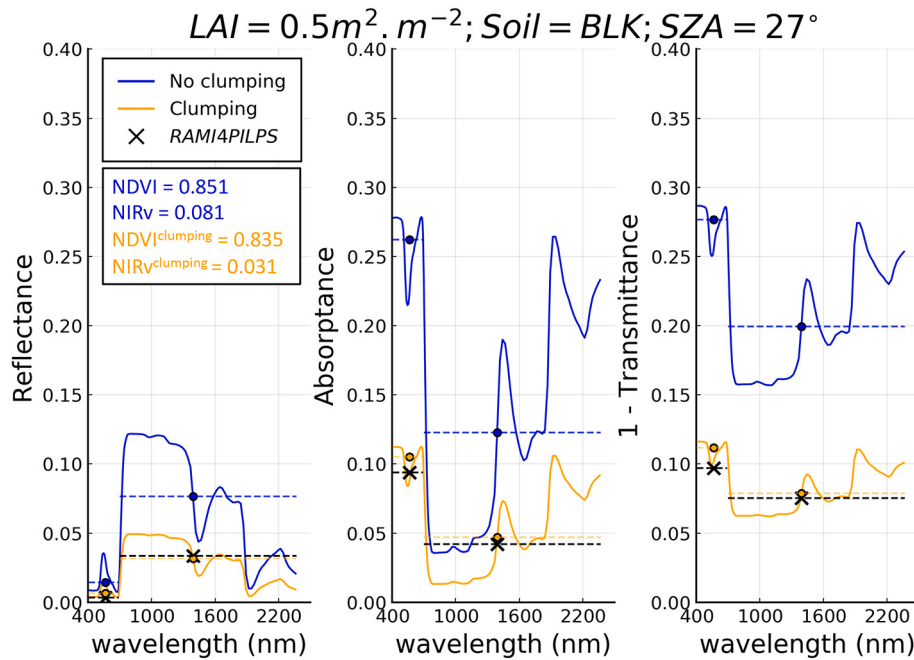
ISS, at Niwot Ridge, Colorado and UMB Station, Michigan, USA.

Fig. 8 shows a scatter plot of far-red SIF (at 757 nm) from CliMA-Land radiative transfer (with clumping in yellow and without clumping in blue) versus far-red SIF derived from OCO-3 for both sites in 2020. The individual points in the linear fit represent the whole scan area shown in Fig. 3. For each OCO-3 overpass, there are several scans for the SAMs. Basically, each scan has very similar sun-sensor geometry and the soundings can be grouped based on phase angle. Each point in Fig. 8 represents the mean of all the soundings with approximately the same phase angle in order to reduce the error associated with sensor geometry.

The estimates of far-red SIF from CliMA-Land radiative transfer with clumping index indicate an improvement with observations. The linear fit between model and observations shows a higher  $r^2$  (0.58 for Niwot Ridge and 0.85 for UMB Station) and a lower RMSE (0.20 for Niwot Ridge and 0.18 for UMB Station) when considering canopy structure with a clumping index, versus the original version of the model without



**Fig. 5.** Intercomparison of reflected, absorbed, and transmitted PAR (400–700 nm) and NIR (700–2500 nm) for 3 canopy densities, 3 soil albedos, and 3 sun zenith angles calculated with 2 different model setups with clumping (orange) and without clumping (blue) (1D) and the RAMI4PILPS reference values (3D) obtained with a 3D Monte Carlo ray-tracing model, raytran.



clumping index. The reduction of 51.2% in RMSE over Niwot Ridge and 21.7% over UMB Station when considering canopy structure through clumping index highlights the importance of considering canopy structure when deriving SIF products from remote sensing.

### 3.4. The impact of canopy clumping on vertical APAR, fAPAR, and NIRv

The radiation partitioning from the CliMA-Land radiative transfer

**Fig. 6.** Intercomparison of reflected, absorbed, and transmitted hyperspectral shortwave radiation (400–2500 nm) for a sparse case ( $LAI = 0.50 \text{ m}^2 \cdot \text{m}^{-2}$  and  $\sim 10\%$  vegetation cover), over black soil, with sun zenith angle =  $27^\circ$  calculated with 2 different model setups with clumping (orange) and without clumping (blue) (1D). The RAMI4PILPS reference values (3D) obtained with a 3D Monte Carlo ray-tracing model, raytran (black crosses represent the average PAR and NIR, separately). The average values for PAR and NIR are shown as points and horizontal dashed lines for clumping (orange) and no clumping (blue). The values of NDVI and NIRv, with and without clumping, are also indicated.

model has been validated against a detailed model benchmarking, as well as the SIF estimates from the model have been tested against SIF observation from remote sensing data. In both cases, results indicate that whenever the clumping index parameterization scheme is considered, the agreement between both, model and highly accurate 3D radiative transfer models, as well as model and satellite observations is higher (RMSE  $\sim 50\%$  smaller).

To further evaluate the impacts of canopy structure on the energy,

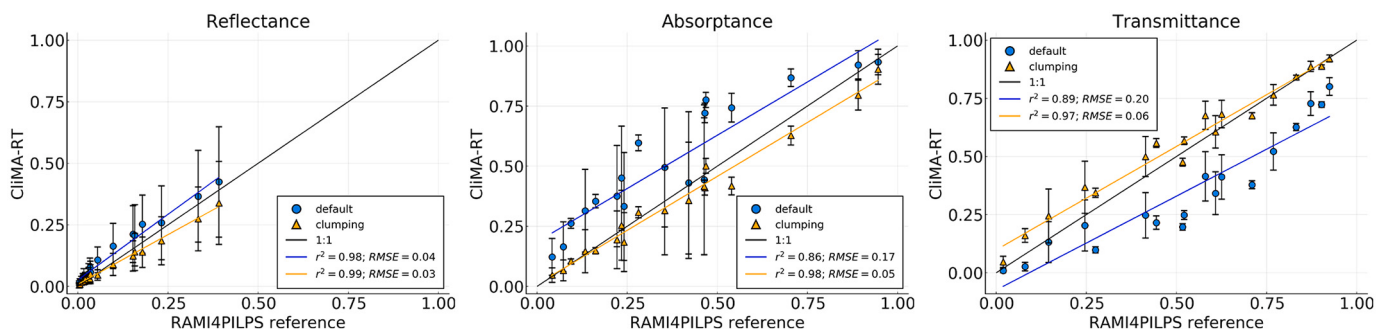


**Fig. 7.** Intercomparison of reflected, absorbed, and transmitted averaged in the PAR (400–700 nm) and NIR (700–2500 nm) wavebands for 3 canopy densities, 3 sun zenith angles, and a black soil albedo calculated with 2 different model setups with clumping (orange) and without clumping (blue) (1D). The RAMI4PILPS reference values (3D) were obtained with a 3D Monte Carlo ray-tracing model, raytran. The vertical black bars indicate the standard deviation of the mean values for each waveband considered in 10 nm spectral resolution.

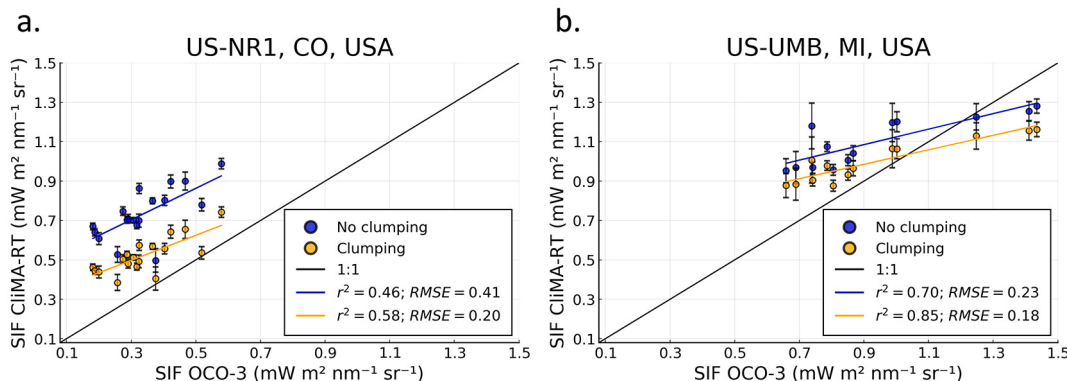


**Fig. 8.** Intercomparison of SIF (757 nm) between CliMA-Land radiative transfer (with clumping in yellow and without clumping in blue) and two SAMs that were taken by OCO-3 at a. Niwot Ridge, Colorado, USA obtained on June 12th and June 16th, 2020, and b. UMB Station, Michigan, USA obtained on August 06th and August 11th, 2020. The  $r^2$  and RMSE of the linear fits are also shown. Each point represents the mean of all the soundings with approximately the same phase angle in order to reduce the error associated with sensor geometry, represented by the error bars.

carbon, and water cycles, the impacts of clumping on vertical fAPAR and APAR should be tested because these variables drive the light limiting regime of photosynthesis in ESMs. Fig. 9 shows the vertical zenith profile of the difference in APAR between the modified CliMA-Land radiative transfer with clumping index minus the default version (without clumping) for 3 canopy densities (0.5, 1.5, and 2.5 m<sup>2</sup>.m<sup>-2</sup>) over 3 soil albedos (BLK, MED, SNW). The CliMA-Land version without clumping is equivalent to the mSCOPE with horizontal canopy structure, and so, the validation with the mSCOPE model is indirectly present in all evaluations.

Throughout all the evaluated scenarios, APAR increases when clumping is considered, with a stronger difference towards the bottom of the evaluated canopy. This result is not straightforward, because the vertical fAPAR does not follow the same behavior as the vertical APAR (see Supplemental material). While the clumping index acts to decrease the total optical depth of the vegetation canopy, fAPAR decreases at the top of the canopy and increases at the bottom. The effect of soil albedo is mostly noted when the value of soil albedo is high (i.e., over SNW with  $\alpha_{soil,PAR} = 0.96$ ), and the zenith angle of incident radiation is small (SZA = 27°), because at nadir the optical pathlength is the shortest. For the sparse canopy, the clumping index reduces the total fAPAR in approximately half of the one obtained by the default CliMA-Land radiative transfer, and the distribution of fAPAR throughout the vertical canopy is homogenous. Over a bright soil, the fAPAR at the bottom of the canopy is relatively larger than at the top because of the scattering effects from the background soil underneath the canopy. This effect has also been shown by Pinty et al. (2006) and Braghieri (2018), whose work reaffirms that for low vegetation densities, fAPAR is rather small and so the

differences between the 1D canopy and the 3D canopy remain limited over a darker soil. For the medium and dense canopies, the clumping index affects the vertical profile of fAPAR in two primary ways: i) it reduces the total amount of PAR absorption at the top layers, and; ii) it increases fAPAR at the bottom of the canopy, especially over brighter soils. Over a bright soil, fAPAR at the bottom of the canopy is more than twice as large as the one calculated by the default version of the model for the dense canopy, and about one and a half times larger than for the medium canopy. This effect is observed throughout all sun zenith angles, with an increase towards larger sun zenith angles.

However, it is expected that although fAPAR decreases in most cases, APAR increases throughout all the evaluated scenes and sun zenith angles because more light penetrates the canopy and, therefore, there is more available energy to be absorbed. For this reason, it is important to evaluate the impacts on fAPAR together with a change in the incident radiation in the top layers of the canopy. In order to keep consistency with reality for the evaluations of vertical APAR, the value of incident PAR at the top of the canopy was modulated following the cosine of the sun zenith angle.

To evaluate the impacts of canopy clumping on the relationships between  $NIR_v$  and  $SIF_{740nm}$  described in Badgley et al. (2017), as well as on the relationship between  $f_{esc}$  and  $NIR_v.fAPAR^{-1}$  as described in Zeng et al. (2019), Eq. (2) was used to recreate multiple canopy densities with different cover fractions, representing a structurally diverse vegetation canopy with LAI varying from 0.01 m<sup>2</sup>.m<sup>-2</sup> to LAI = 4.50 m<sup>2</sup>.m<sup>-2</sup>, and vegetation cover fraction calculated as LAI over 5. All scenes were simulated over all possible sun zenith angles with background soil albedo set to black (BLK; 0.0).

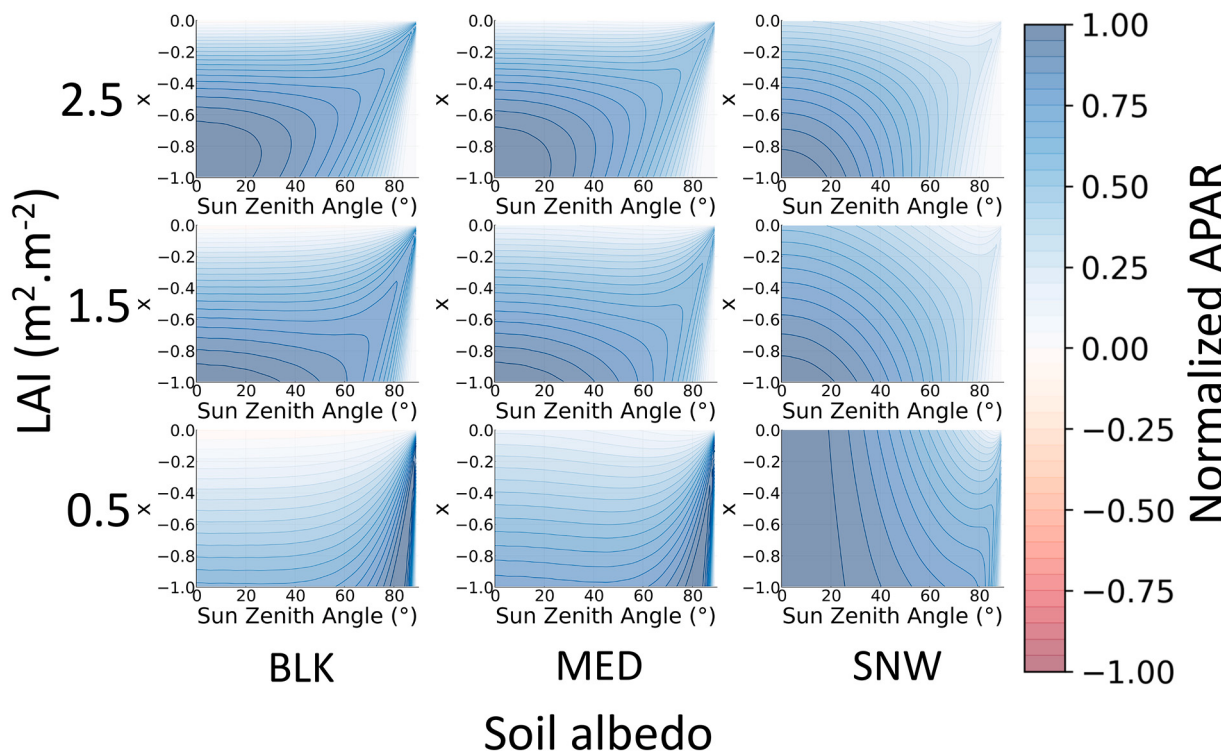


**Fig. 9.** Vertical zenith profile of normalized APAR difference between the modified CliMA-Land radiative transfer with clumping index minus the non-clumping version for 3 canopy densities ( $0.5, 1.5$ , and  $2.5\text{ m}^2\cdot\text{m}^{-2}$ ) over 3 soil albedos (BLK, MED, SNW). x is the relative optical height, which runs from -1 at the bottom to zero at the top of the canopy.

**Fig. 10a.** shows the linear fit between calculated SIF<sub>740nm</sub> versus NIR<sub>v</sub> for the modified CliMA-Land radiative transfer with clumping index (in yellow) and the default version (in blue) for multiple canopy densities. The consideration of canopy clumping improves the relationship between estimated SIF and NIR<sub>v</sub> from the CliMA-Land radiative transfer model, with an increase in  $r^2$  from 0.89 to 0.94, and a decrease in RMSE from  $2.21\text{ mWm}^2\text{nm}^{-1}\text{sr}^{-1}$  to  $1.75\text{ mWm}^2\text{nm}^{-1}\text{sr}^{-1}$ . While **Fig. 10b.** shows the linear fit between  $f_{esc}$  and the  $\text{NIR}_v/\text{FAPAR}^{-1}$  for the modified CliMA-Land radiative transfer with clumping index and the default version for multiple canopy densities (from LAI =  $0.01\text{ m}^2\cdot\text{m}^{-2}$  to LAI =  $4.50\text{ m}^2\cdot\text{m}^{-2}$ ) over a black soil albedo (BLK) with clumping calculated through Eq. (2) for sun zenith angles from  $0^\circ$  to  $30^\circ$ . For

similar figures over medium (MED) and snow (SNW) soil albedos, see Supplemental material. The linear fit improves when canopy clumping is considered with an increased  $r^2$  values from 0.78 to 0.83. While the RMSE value decreased for the linear relationship when the clumping index was considered, the relationship described in Zeng et al. (2019) does not refer to an absolute equal equation, but rather to an approximation of  $f_{esc}$  and  $\text{NIR}_v/\text{FAPAR}^{-1}$ , and so, the absolute values should not be strictly considered.

In **Fig. 10b.**, the linear fit of the CliMA-Land radiative transfer without clumping index has AIC = -4923.44 and BIC = -4907.90, while the version with clumping index has AIC = -5291.47 and the BIC = -5275.94. The AIC and BIC values indicate a stronger relationship

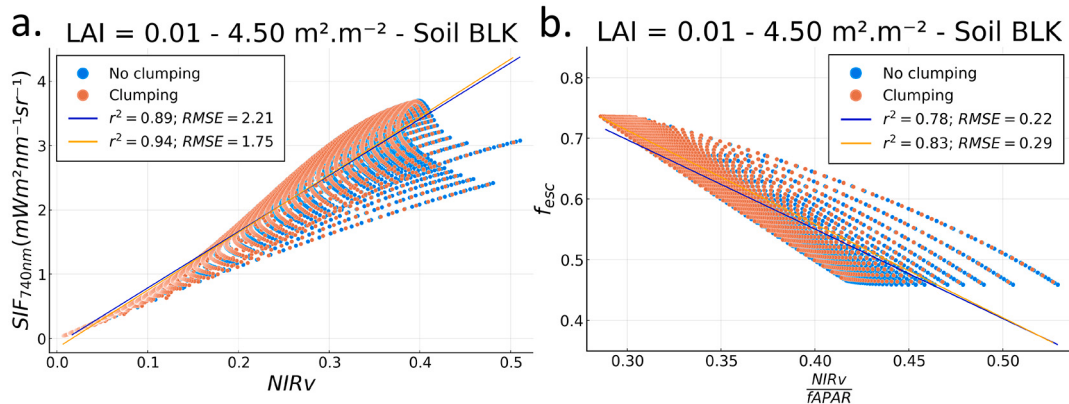


**Fig. 10.** a. Linear fit between SIF<sub>740nm</sub> and NIR<sub>v</sub> for the modified CliMA-Land radiative transfer with clumping index (yellow) and the default version (blue) for multiple canopy densities (from LAI =  $0.01\text{ m}^2\cdot\text{m}^{-2}$  to LAI =  $4.50\text{ m}^2\cdot\text{m}^{-2}$ ) over a black soil albedo (BLK) with clumping calculated through Eq. (2) for sun zenith angles from  $0^\circ$  to  $89^\circ$ , and; b. linear fit between the fluorescence escape ratio ( $f_{esc}$ ) and the  $\text{NIR}_v/\text{FAPAR}$  for the modified CliMA-Land radiative transfer with clumping index and the default version for multiple canopy densities and over a black soil albedo (BLK) as in **Fig. 10a.** with clumping calculated through Eq. (2) for sun zenith angles from  $0^\circ$  to  $30^\circ$ . For CliMA-Land radiative transfer without clumping index the AIC = -4923.44 and the BIC = -4907.90, while for CliMA-Land radiative transfer with clumping index the AIC = -5291.47 and the BIC = -5275.94.

between  $f_{esc}$  and  $NIR_v \cdot fAPAR^{-1}$ , as proposed by Zeng et al. (2019), when canopy structure is considered.

#### 4. Discussion

In this study, we implemented and evaluated a parameterization of horizontal vegetation structure on the radiative transfer scheme of a new generation ESM, the CliMA model. We benchmarked the radiation partitioning of CliMA-Land radiative transfer with results from a 3D Monte-Carlo ray tracer previously presented in Widlowski et al. (2011). In each of the evaluated scenarios, all terms of the radiation partitioning (reflectance, absorptance, and transmittance) from the model version that included the effects of canopy structure showed a better agreement with the accurate 3D modeling, indicating the importance of considering not only the vertical heterogeneity of vegetation canopies, but also the horizontal effects of canopy structure. The improvement for reflectance was smaller than the ones for absorptance and transmittance partly due to the fact that reflectance values are the smallest terms of the radiation partitioning for the evaluated cases.

The main difference between the present study and previous ones is the hyperspectral nature of the radiative transfer model combined with horizontal canopy structural heterogeneity in CliMA-Land. By using a single value of clumping index following the work of Pinty et al. (2006), we were able to account for the effects of vegetation structure on the transfer of radiation across all wavelengths of the shortwave radiation spectrum with 10 nm spectral resolution. The results presented here highlight the capability of the new CliMA-Land model to be directly compared with observed canopy spectroscopy from high resolution spectral data currently available from aircrafts, preparing Earth System modelers for a suite of global hyperspectral measurements that soon will be available from the US SBG mission (Cawse-Nicholson et al., 2021; Schimel and Schneider, 2019).

We also presented a validation exercise with observations of SIF emission over an evergreen needleleaf site and a deciduous broadleaf site in the USA from remote sensing with the recently launched OCO-3 sensor on board of the ISS at spatial resolution of not more than 4 km, including the footprint of two flux tower sites (US-NR1 and US-UMB), in order to facilitate further evaluation and comparison to FLUXNET data (Baldocchi et al., 2001). Combining SIF from OCO-3 with a suite of remote sensing products, including Copernicus LAI (Fuster et al., 2020) at 300 m spatial resolution, a chlorophyll product from ENVISAT MERIS (Croft et al., 2020), and clumping index from MODIS (He et al., 2012), we were able to determine a substantial improvement on modeled SIF when vegetation canopy structure was considered. The importance of directly modeling SIF with an ESM is related to the SIF-GPP relationships required for remote large-scale estimations of GPP (Ryu et al., 2019; Dechant et al., 2020), as well as the direct assimilation of SIF data to improve GPP predictions (Norton et al., 2019; Parazoo et al., 2020), which are currently highly uncertain globally (Braghieri et al., 2019) (see Supplemental material for a model intercomparison with other SIF-enabled LSMS). SIF<sub>740 nm</sub> estimates from CliMA-Land are comparable to those of BETHY, while the impact of clumping decreases the total SIF signal. In the comparison with SCOPE, CliMA-Land slightly underestimates the SIF peak.

After thorough validation with accurate 3D modeling and observations, we evaluated the impact of the clumping index parameterization scheme on proxies of GPP, i.e., vertical APAR, in order to characterize further impacts on GPP from CliMA-Land when absorbed radiation will be used to derived photosynthesis through the Farquhar-von Caemmerer-Berry model (Farquhar et al., 1980). Contrary to expectation, considering horizontal canopy structure through the addition of clumping on the radiative transfer scheme of CliMA-Land caused fAPAR to vary largely across different canopy densities, illumination angles, and soil background albedos, but with one single impact on the total APAR across the vertical canopy. Throughout all the evaluated scenes, APAR increased when canopy structure is considered, especially in the

bottom layers of the vegetation canopy. This can be thought of as a reduction on the total optical depth of the canopy and, therefore, less plant material for the radiation to interact with along its pathway to the ground and back up after interacting with the surface underneath. These results are in alignment with previous studies that evaluated the impact of the clumping index on radiative transfer schemes in land surface models (Braghieri et al., 2020; Braghieri et al., 2019; Loew et al., 2014).

The CliMA-Land model can simulate photosynthesis. However, photosynthesis is a process that includes many more different sub-models, e.g., the Farquhar ecophysiology model (Farquhar et al., 1980), model of root development, model of water distribution in soils and plants. Therefore, the current study is limited to the evaluation of the radiative transfer scheme in CliMA-Land, in order to keep consistency and conciseness without completely leaving photosynthesis behind through the evaluation of the impact of clumping on vegetation indices. Nevertheless, further evaluation on CliMA-Land photosynthesis is required.

Finally, we tested two relationships that were described in the literature as strongly influenced by canopy structure and that our new model allowed us to explore. The first one is the relationship between observed SIF and  $NIR_v$  proposed by Badgley et al. (2017) and further evaluated in a number of studies (Badgley et al., 2019; Dechant et al., 2020). Here we showed an improved linear fit between  $NIR_v$  and SIF when considering canopy structure to calculate the transfer of radiation with a reduction of 20% on RMSE. This result reinforces previous evidence relating the effect of canopy structure, represented by  $f_{esc}$ , on SIF emission, APAR, and GPP using modeling and observations (Dechant et al., 2020; Du et al., 2017; Migliavacca et al., 2017).

The impacts of canopy clumping were also evaluated on the relationship demonstrated by Zeng et al. (2019) and described in Eq. (5) where  $f_{esc}$  can be approximated by  $NIR_v \cdot fAPAR^{-1}$ . Zeng et al. (2019) showed that  $f_{esc}$  can be derived from  $NIR_v$  properly even over sparsely vegetated areas with minimal effects from background soil albedo. In here, we showed an improved linear fit in Fig. 10b when considering clumping index in CliMA-Land radiative transfer, which highlights the important effect that horizontal canopy heterogeneity can have on the appropriate usage of Eq. (5).

##### 4.1. Data uncertainties and model limitations

The non-linearity of clumping index spatial scaling at the landscape level has been previously explored using LAI-2000 and digital hemispherical photography datasets (Ryu et al., 2010a). In our study, the clumping index and LAI values were linearly scaled up as area weighted averages for the OCO-3 SIF validation experiment (<4 km vs. 500 m), which may introduce biases in our results, mainly due to changes in vegetation heterogeneity with spatial scale. The linear averaging method in this particular case was preferred due to: (i) the absence of high-resolution gap fraction and clumping index measurements; and, (ii) the fairly homogeneous clumping index values in the evaluated areas (see Supplemental material). In addition, the MODIS clumping index was retrieved using the Normalized Difference between Hotspot and Darkspot (NDHD) algorithm (Chen et al., 2005) and validated with *in-situ* measurements over a set of 63 globally distributed LPV (Land Product Validation) and VALERI (VALidation of Land European Remote sensing Instruments) sites (Baret et al., 2006; Garrigues et al., 2008; Nightingale et al., 2011; Pisek et al., 2015b), as well as intercompared with higher resolution (275 m) data from the Multi-angle Imaging SpectroRadiometer (MISR) satellite (Pisek et al., 2013), showing a particularly good agreement over needleleaf forests, with MODIS showing a wider range of clumping index values (0.47–0.72) compared to MISR (0.52–0.59) (Pisek et al., 2015b).

Further intercomparison between MISR, MODIS, and POLDER clumping index datasets (Pisek et al., 2010) highlighted the importance of appropriately scaling up the clumping index values in order to match the scale of the application. For instance, if POLDER clumping index

(~6 km resolution) was to be used with our model, an alternative scaling methodology would be preferred in order to avoid the addition of significant biases due to the usage of coarser resolution data. Likewise, if an evaluation was to be performed using OCO-3 SIF grouped into larger areas (e.g., 0.5 degree as current ESMs), a non-linear averaging method would be indicated in order to limit uncertainty (Ryu et al., 2010a). In future validation studies of CliMA-Land at site level with scanning spectrometers, e.g., PhotoSpec (Grossmann et al., 2018), clumping index values should be derived at much finer spatial scales (<1 m), taking into account clumping index variations with canopy height and view zenith/azimuth angles accordingly.

## 5. Conclusion

Our work suggests that considering vertical and horizontal vegetation canopy structure through the addition of a clumping index parameterization scheme may significantly improve the hyperspectral shortwave radiation partitioning of an ESM without losing efficiency, with a RMSE reduction on the order of 25% for reflectance, 66% for absorptance, and 75% for transmittance in comparison to a highly accurate Monte Carlo 3D radiative transfer model. The dominant effect that introducing clumping has in our study is to allow more shortwave radiation to propagate further into lower canopy layers increasing APAR values throughout the vertical canopy and across sun zenith angles.

We also compared SIF emissions against observed data with a satellite spectrometer, NASA's OCO-3. The results presented here strongly support previous evidence that horizontal canopy structural features are crucial for an accurate estimation of SIF, as do further extrapolations that might come out from this variable, such as global photosynthesis. The improvement of SIF estimates with a clumping index indicates that the clumping index can capture the horizontal canopy structural features at remote sensing scales (<4 km).

Finally, we showed how the clumping index parameterization scheme improved the SIF correlation to  $\text{NIR}_v$ , as well the correlation of  $f_{\text{esc}}$  with fAPAR, which provides further evidence for the role of vertical and horizontal canopy structure on SIF emission and the appropriate determination of other vegetation indices.

## Data availability

The CliMA project, code, simulation configurations, model output, and tools to work with the output are described at <https://github.com/CliMA>. The CliMA-land model and examples are available at

## Appendix A. Appendix

### A.1. Calculating escape and recollision probabilities

This Appendix has additional information on the calculation of the escape and recollision probabilities. For the complete set of equations, see Huang et al. (2007) and Smolander and Stenberg (2005). First, the canopy interception ( $i$ ) refers to the probability of an incoming photon interacting with the vegetation canopy, and it can be approximated by  $1 - P_{\text{gap}}$ , where  $P_{\text{gap}}$  is the direct transmittance. Second, the recollision probability ( $p$ ) refers to the probability that a photon recollides with elements of the canopy at an n-th plus one time, on its n-th interaction with the canopy, and it can be obtained by rearranging Eq. (2) presented in Smolander and Stenberg (2005) as:

$$p_{s/d} = \frac{1 - \left( \frac{1-\omega_l}{fAPAR_{s/d}} \right) \times (1 - P_{\text{gap}})}{\omega_l} \quad (\text{A1})$$

where fAPAR is the fraction of absorbed PAR,  $P_{\text{gap}}$  is the direct transmittance, and  $\omega_l$  is the single scattering albedo. Finally, the escape probability ( $\rho$ ) refers to the probability of a photon escaping the vegetation canopy after interacting with elements of vegetation, and it can be obtained by rearranging Eq. (9) presented in Huang et al. (2007) as:

$$\rho_{s/d} = \frac{R_{s/d}}{\omega_l \times (1 - P_{\text{gap}}) + \frac{\omega_l^2 \times p_{s/d} \times (1 - P_{\text{gap}})}{1 - p_{s/d} \times \omega_l}} \quad (\text{A2})$$

<https://github.com/CliMA/Land>. The minimization of hyperspectral leaf reflectance and transmittance was performed using a Julia package available at <https://github.com/Yujie-W/ConstrainedRootSolvers.jl>. The LAI map, PROBA-V LAI V2, was produced by Copernicus at 1 km resolution and it is available at <https://land.copernicus.eu/global/products/lai>. National Ecological Observatory Network, 2020. Data Product DP3.30011.001, Albedo - spectrometer - mosaic. Provisional data downloaded from <https://data.neonscience.org> on November 30, 2020. Battelle, Boulder, CO, USA NEON. 2020.

## Description of author's responsibilities

RKB: conceptualization, methodology, formal analysis, writing - original draft, writing - review & editing, implementation of clumping index, research; RKB and YW: spectral properties fitting package, model coding, and writing; RKB and RD: OCO-3 SIF methodology and writing; DS: soil spectral properties for Niwot Ridge; TM and JLW: validation datasets and editing; ML, AB, JW, PG: editing and model conceptualization; CF: model conceptualization, coding, review, and editing.

## Declaration of Competing Interest

The authors declare no competing interests.

## Acknowledgments

This research was carried out at the Jet Propulsion Laboratory, California Institute of Technology, under a contract with the National Aeronautics and Space Administration, California Institute of Technology. Government sponsorship acknowledged. Copyright 2021. All rights reserved. TSM and CF are supported by the National Aeronautics and Space Administration (80NSSC19M0129) and the National Science Foundation, through the Macrosystems Biology and NEON Enabled Science Program (DEB579 1926090). Part of this research was funded by Eric and Wendy Schmidt by recommendation of the Schmidt Futures program, and by Hopewell Fund. RD is supported by NASA Making Earth System Data Records for Use in Research Environments (MEASUREs) Program (NNN12AA01C) and OCO-2/3 Science Team (80NSSC18K0895). We would like to thank Nick Parazoo for sharing model runs from the SIF-enabled LSMs for Niwot Ridge. We thank the editors and three anonymous reviewers whose suggestions helped improve this manuscript.

where R is the canopy albedo,  $P_{gap}$  is the direct transmittance,  $\omega_l$  is the single scattering albedo, and p is the recollision probability.

## Appendix B. Supplementary data

Supplementary data to this article can be found online at <https://doi.org/10.1016/j.rse.2021.112497>.

## References

- Aho, K., Derryberry, D., Peterson, T., 2014. Model selection for ecologists: the worldviews of AIC and BIC. *Ecology* 95, 631–636. <https://doi.org/10.1890/13-1452.1>.
- Akaike, H., 1973. Information theory and an extension of the maximum likelihood principle. In: Kaido, A. (Ed.), *Second International Symposium on Information Theory*. Budapest, Hungary, pp. 267–281.
- Arora, V.K., Katavouta, A., Williams, R.G., Jones, C.D., Brovkin, V., Friedlingstein, P., Schwinger, J., Bopp, L., Boucher, O., Cadule, P., Chamberlain, M.A., Christian, J.R., Delire, C., Fisher, R.A., Hajima, T., Ilyina, T., Joetzer, E., Kawamiya, M., Koven, C. D., Krasting, J.P., Law, R.M., Lawrence, D.M., Lenton, A., Lindsay, K., Pontratz, J., Raddatz, T., Séférian, R., Tachiiri, K., Tjiputra, J.F., Wilshire, A., Wu, T., Ziehn, T., 2020. Carbon-concentration and carbon-climate feedbacks in CMIP6 models and their comparison to CMIP5 models. *Biogeosciences* 17, 4173–4222. <https://doi.org/10.5194/bg-17-4173-2020>.
- Badgley, G., Field, C.B., Berry, J.A., 2017. Canopy near-infrared reflectance and terrestrial photosynthesis. *Sci. Adv.* 3, e1602244 <https://doi.org/10.1126/sciadv.1602244>.
- Badgley, G., Anderegg, L.D.L., Berry, J.A., Field, C.B., 2019. Terrestrial gross primary production: using NIR V to scale from site to globe. *Glob. Chang. Biol.* 25, 3731–3740. <https://doi.org/10.1111/gcb.14729>.
- Baldocchi, D.D., Harley, P.C., 1995. Scaling carbon dioxide and water vapour exchange from leaf to canopy in a deciduous forest. II. Model testing and application. *Plant Cell Environ.* 18, 1157–1173. <https://doi.org/10.1111/j.1365-3040.1995.tb00626.x>.
- Baldocchi, D., Falge, E., Gu, L., Olson, R., Hollinger, D., Running, S., Anthoni, P., Bernhofer, C., Davis, K., Evans, R., Fuentes, J., Goldstein, A., Katul, G., Law, B., Lee, X., Malhi, Y., Meyers, T., Munger, W., Oechel, W., Paw, U.K.T., Pilegaard, K., Schmid, H.P., Valentini, R., Verma, S., Vesala, T., Wilson, K., Wofsy, S., 2001. FLUXNET: a new tool to study the temporal and spatial variability of ecosystem-scale carbon dioxide, water vapor, and energy flux densities. *Bull. Am. Meteorol. Soc.* [https://doi.org/10.1175/1520-0477\(2001\)082<2415:FANTTS>2.3.CO;2](https://doi.org/10.1175/1520-0477(2001)082<2415:FANTTS>2.3.CO;2).
- Baldocchi, D.D., Wilson, K.B., Gu, L., 2002. How the environment, canopy structure and canopy physiological functioning influence carbon, water and energy fluxes of a temperate broad-leaved deciduous forest—an assessment with the biophysical model CANOAK. *Tree Physiol.* 22, 1065–1077.
- Baret, F., Morissette, J.T., Fernandes, R.A., Champeaux, J.L., Myneni, R.B., Chen, J., Plummer, S., Weiss, M., Bacour, C., Garrigues, S., Nickeson, J.E., 2006. Evaluation of the representativeness of networks of sites for the global validation and intercomparison of land biophysical products: proposition of the CEOS-BELMANIP. *IEEE Trans. Geosci. Remote Sens.* 44, 1794–1802. <https://doi.org/10.1109/TGRS.2006.876030>.
- Blanken, P.D., Williams, M.W., Burns, S.P., Monson, R.K., Knowles, J., Chowanski, K., Ackerman, T., 2009. A comparison of water and carbon dioxide exchange at a windy alpine tundra and subalpine forest site near Niwot Ridge, Colorado. *Biogeochemistry* 95, 61–76. <https://doi.org/10.1007/s10533-009-9325-9>.
- Bonan, G.B., Doney, S.C., 2018. Climate, ecosystems, and planetary futures: the challenge to predict life in Earth system models. *Science* (80-. ) 359, eaam8328. <https://doi.org/10.1126/science.aam8328>.
- Bonan, G.B., Patton, E.G., Finnigan, J.J., Baldocchi, D.D., Harman, I.N., 2021. Moving beyond the incorrect but useful paradigm: reevaluating big-leaf and multilayer plant canopies to model biosphere-atmosphere fluxes – a review. *Agric. For. Meteorol.* 306, 108435. <https://doi.org/10.1016/j.agrformet.2021.108435>.
- Bowling, D.R., Logan, B.A., Hufkens, K., Aubrecht, D.M., Richardson, A.D., Burns, S.P., Anderegg, W.R.L., Blanken, P.D., Eiriksson, D.P., 2018. Limitations to winter and spring photosynthesis of a Rocky Mountain subalpine forest. *Agric. For. Meteorol.* 252, 241–255. <https://doi.org/10.1016/j.agrformet.2018.01.025>.
- Braghieri, R.K., 2018. Improving the Treatment of Vegetation Canopy Architecture in Radiative Transfer Schemes. University of Reading, UK.
- Braghieri, R.K., Quaife, T., Black, E., He, L., Chen, J.M., 2019. Underestimation of global photosynthesis in Earth system models due to representation of vegetation structure. *Global Biogeochem. Cycles*, 2018GB006135. <https://doi.org/10.1029/2018GB006135>.
- Braghieri, R.K., Quaife, T., Black, E., Ryu, Y., Chen, Q., De Kauwe, M.G., Baldocchi, D., 2020. Influence of sun zenith angle on canopy clumping and the resulting impacts on photosynthesis. *Agric. For. Meteorol.* 291, 108065 <https://doi.org/10.1016/j.agrformet.2020.108065>.
- Burggraaff, O., 2020. Biases from incorrect reflectance convolution. *Opt. Express* 28, 13801. <https://doi.org/10.1364/oe.391470>.
- Burns, S.P., Blanken, P.D., Turnipseed, A.A., Hu, J., Monson, R.K., 2015. The influence of warm-season precipitation on the diel cycle of the surface energy balance and carbon dioxide at a Colorado subalpine forest site. *Biogeosciences* 12, 7349–7377. <https://doi.org/10.5194/bg-12-7349-2015>.
- Butler, E.E., Datta, A., Flores-Moreno, H., Chen, M., Wythers, K.R., Fazayeli, F., Banerjee, A., Atkin, O.K., Kattge, J., Amiaud, B., Blonder, B., Boenisch, G., Bond-Lamberty, B., Brown, K.A., Byun, C., Campetella, G., Cerabolini, B.E.L., Cornelissen, J.H.C., Craine, J.M., Craven, D., De Vries, F.T., Díaz, S., Domingues, T. F., Forey, E., González-Melo, A., Gross, N., Han, W., Hattingh, W.N., Hickler, T., Jansen, S., Kramer, K., Kraft, N.J.B., Kurokawa, H., Laughlin, D.C., Meir, P., Minden, V., Niinemets, Ü., Onoda, Y., Peñuelas, J., Read, Q., Sack, L., Schamp, B., Soudzilovskaya, N.A., Spasojevic, M.J., Sosinski, E., Thornton, P.E., Valladares, F., Van Bodegom, P.M., Williams, M., Wirth, C., Reich, P.B., Schlesinger, W.H., 2017. Mapping local and global variability in plant trait distributions. *Proc. Natl. Acad. Sci. U. S. A.* 114, E10937–E10946. <https://doi.org/10.1073/pnas.1708984114>.
- Cawse-Nicholson, K., Townsend, P.A., Schimel, D., Assiri, A.M., Blake, P.L., Buongiorno, M.F., Campbell, P., Carmon, N., Casey, K.A., Correa-Pabón, R.E., Dahlén, K.M., Dashti, H., Dennison, P.E., Dierssen, H., Erickson, A., Fisher, J.B., Frouin, R., Gatebe, C.K., Gholizadeh, H., Gierach, M., Glenn, N.F., Goodman, J.A., Griffith, D.M., Guild, L., Hakkenberg, C.R., Hochberg, E.J., Holmes, T.R.H., Hu, C., Hulley, G., Huemmrich, K.F., Kudela, R.M., Kokaly, R.F., Lee, C.M., Martin, R., Miller, C.E., Moses, W.K., Muller-Karger, F.E., Ortiz, J.D., Otis, D.B., Pahlevan, N., Painter, T.H., Pavlick, R., Poultier, B., Qi, Y., Realimuto, V.J., Roberts, D., Schaeppman, M.E., Schneider, F.D., Schwandner, F.M., Serbin, S.P., Shiklomanov, A. N., Stavros, E.N., Thompson, D.R., Torres-Perez, J.L., Turpie, K.R., Tzortziou, M., Ustin, S., Yu, S., Yusup, Y., Zhang, Q., the SBG Algorithms Working Group, 2021. NASA's surface biology and geology designated observable: A perspective on surface imaging algorithms. *Remote Sens. Environ.* 257. <https://doi.org/10.1016/j.rse.2021.112349>.
- Cescatti, A., 1997. Modelling the radiative transfer in discontinuous canopies of asymmetric crowns. II. Model testing and application in a Norway spruce stand. *Ecol. Modell.* 101, 275–284.
- Chen, J.M., Cihlar, J., 1995. Quantifying the effect of canopy architecture on optical measurements of leaf area index using two gap size analysis methods. *IEEE Trans. Geosci. Remote Sens.* 33, 777–787. <https://doi.org/10.1109/36.387593>.
- Chen, J.M., Menges, C.H., Leblanc, S.G., 2005. Global mapping of foliage clumping index using multi-angular satellite data. *Remote Sens. Environ.* 97, 447–457.
- Chen, J.M., Mo, G., Pisek, J., Liu, J., Deng, F., Ishizawa, M., Chan, D., 2012. Effects of foliage clumping on the estimation of global terrestrial gross primary productivity. *Glob. Biogeochem. Cycles* 26.
- Cheng, R., Magney, T.S., Dutta, D., Bowling, D.R., Logan, B.A., Burns, S.P., Blanken, P.D., Grossmann, K., Lopez, S., Richardson, A.D., Stutz, J., Frankenber, C., 2020. Decomposing reflectance spectra to track gross primary production in a subalpine evergreen forest. *Biogeosciences* 17, 4523–4544. <https://doi.org/10.5194/bg-17-4523-2020>.
- Croft, H., Chen, J.M., Wang, R., Mo, G., Luo, S., Luo, X., He, L., Gonsamo, A., Arabian, J., Zhang, Y., Simic-Milas, A., Noland, T.L., He, Y., Homolová, L., Malenovský, Z., Yi, Q., Beringer, J., Amiri, R., Hutley, L., Arellano, P., Stahl, C., Bonal, D., 2020. The global distribution of leaf chlorophyll content. *Remote Sens. Environ.* 236, 111479. <https://doi.org/10.1016/j.rse.2019.111479>.
- Dechant, B., Ryu, Y., Kang, M., 2019. Making full use of hyperspectral data for gross primary productivity estimation with multivariate regression: mechanistic insights from observations and process-based simulations. *Remote Sens. Environ.* 234, 111435. <https://doi.org/10.1016/j.rse.2019.111435>.
- Dechant, B., Ryu, Y., Badgley, G., Zeng, Y., Berry, J.A., Zhang, Y., Goulas, Y., Li, Z., Zhang, Q., Kang, M., Li, J., Moya, I., 2020. Canopy structure explains the relationship between photosynthesis and sun-induced chlorophyll fluorescence in crops. *Remote Sens. Environ.* 241, 111733. <https://doi.org/10.1016/j.rse.2020.111733>.
- Dorman, J.L., Sellers, P.J., 1989. A global climatology of albedo, roughness length and stomatal resistance for atmospheric general circulation models as represented by the Simple Biosphere Model (SiB). *J. Appl. Meteorol.* 28, 833–855. [https://doi.org/10.1175/1520-0450\(1989\)028<0833:AGCOAR>2.0.CO;2](https://doi.org/10.1175/1520-0450(1989)028<0833:AGCOAR>2.0.CO;2).
- Doughty, R., Köhler, P., Frankenber, C., Magney, T.S., Xiao, X., Qin, Y., Wu, X., Moore, B., 2019. TROPOMI reveals dry-season increase of solar-induced chlorophyll fluorescence in the Amazon forest. *Proc. Natl. Acad. Sci.* 116, 22393–22398. <https://doi.org/10.1073/pnas.1908157116>.
- Du, S., Liu, L., Liu, X., Hu, J., 2017. Response of canopy solar-induced chlorophyll fluorescence to the absorbed photosynthetically active radiation absorbed by chlorophyll. *Remote Sens.* 9, 911. <https://doi.org/10.3390/rs9090911>.
- Butta, D., Schimel, D.S., Sun, Y., Van Der Tol, C., Frankenber, C., 2019. Optimal inverse estimation of ecosystem parameters from observations of carbon and energy fluxes. *Biogeosciences* 16, 77–103. <https://doi.org/10.5194/bg-16-77-2019>.
- Duursma, R.A., Medlyn, B.E., 2012. MAESPA: a model to study interactions between water limitation, environmental drivers and vegetation function at tree and stand levels, with an example application to [CO<sub>2</sub>] x drought interactions. *Geosci. Model Dev.* 5, 919–940.
- Eldering, A., Taylor, T.E., O'Dell, C.W., Pavlick, R., 2019. The OCO-3 mission: measurement objectives and expected performance based on 1 year of simulated data. *Atmos. Meas. Tech.* 12, 2341–2370. <https://doi.org/10.5194/amt-12-2341-2019>.
- Fang, H., Liu, W., Li, W., Wei, S., 2018. Estimation of the directional and whole apparent clumping index (ACI) from indirect optical measurements. *ISPRS J. Photogramm. Remote Sens.* 144, 1–13. <https://doi.org/10.1016/j.isprsjprs.2018.06.022>.

- Farquhar, G.D., Caemmerer, S., Berry, J.A., 1980. A biochemical model of photosynthetic CO<sub>2</sub> assimilation in leaves of C3 species. *Planta* 149, 78–90. <https://doi.org/10.1007/BF00386231>.
- Féret, J.-B., Gitelson, A.A., Noble, S.D., Jacquemoud, S., 2017a. PROSPECT-D: towards modeling leaf optical properties through a complete lifecycle. *Remote Sens. Environ.* 193, 204–215. <https://doi.org/10.1016/j.rse.2017.03.004>.
- Féret, J.B., Gitelson, A.A., Noble, S.D., Jacquemoud, S., 2017b. PROSPECT-D: towards modeling leaf optical properties through a complete lifecycle. *Remote Sens. Environ.* 193, 204–215. <https://doi.org/10.1016/j.rse.2017.03.004>.
- Féret, J.B., le Maire, G., Jay, S., Berveiller, D., Bendoula, R., Hmimina, G., Cheraiet, A., Oliveira, J.C., Ponzoni, F.J., Solanki, T., de Boissieu, F., Chave, J., Nouvellon, Y., Porcar-Castell, A., Poisy, C., Soudani, K., Gastellu-Etchegorry, J.P., Lefèvre-Fonollosa, M.J., 2019. Estimating leaf mass per area and equivalent water thickness based on leaf optical properties: potential and limitations of physical modeling and machine learning. *Remote Sens. Environ.* 231, 110959. <https://doi.org/10.1016/j.rse.2018.11.002>.
- Fournier, A., Daumard, F., Champagne, S., Ounis, A., Goulas, Y., Moya, I., 2012. Effect of canopy structure on sun-induced chlorophyll fluorescence. *ISPRS J. Photogramm. Remote Sens.* 68, 112–120. <https://doi.org/10.1016/j.isprsjprs.2012.01.003>.
- Frankenberg, C., O'Dell, C., Berry, J., Guanter, L., Joiner, J., Köhler, P., Pollock, R., Taylor, T.E., 2014. Prospects for chlorophyll fluorescence remote sensing from the Orbiting Carbon Observatory-2. *Remote Sens. Environ.* 147, 1–12. <https://doi.org/10.1016/j.rse.2014.02.007>.
- Friedlingstein, P., Meinshausen, M., Arora, V.K., Jones, C.D., Anav, A., Liddicoat, S.K., Knutti, R., 2014. Uncertainties in CMIP5 climate projections due to carbon cycle feedbacks. *J. Clim.* 27, 511–526. <https://doi.org/10.1175/JCLI-D-12-00579.1>.
- Friedlingstein, P., O'Sullivan, M., Jones, M.W., Andrew, R.M., Hauck, J., Olsen, A., Peters, G.P., Peters, W., Pongratz, J., Sitch, S., Le Quéré, C., Canadell, J.G., Ciais, P., Jackson, R.B., Alin, S., Aragão, L.E.O.C., Arneth, A., Arora, V., Bates, N.R., Becker, M., Benoit-Cattin, A., Bittig, H.C., Bopp, L., Bultan, S., Chandra, N., Chevallier, F., Chini, L.P., Evans, W., Florentie, L., Forster, P.M., Gasser, T., Gehlen, M., Gilfillan, D., Grätzl, T., Gregor, L., Gruber, N., Harris, I., Hartung, K., Haverd, V., Houghton, R.A., Ilyina, T., Jain, A.K., Joetzer, E., Kadono, K., Kato, E., Kitidis, V., Korsbakken, J.I., Landschützer, P., Lefèvre, N., Lenton, A., Liébert, S., Liu, Z., Lombardozzi, D., Marland, G., Metzl, N., Munro, D.R., Nabel, J.E.M.S., Nakaoaka, S.-I., Niwa, Y., O'Brien, K., Ono, T., Palmer, P.L., Pierrot, D., Poulet, B., Resplandy, L., Robertson, E., Rödenbeck, C., Schwinger, J., Séférian, R., Skjelvan, I., Smith, A.J.P., Sutton, A.J., Tanhua, T., Tans, P.P., Tian, H., Tilbrook, B., van der Werf, G., Vuichard, N., Walker, A.P., Wanninkhof, R., Watson, A.J., Willis, D., Wiltshire, A.J., Yuan, W., Yue, X., Zachele, S., 2020. Global carbon budget 2020. *Earth Syst. Sci. Data* 12, 3269–3340. <https://doi.org/10.5194/essd-12-3269-2020>.
- Fuster, B., Sánchez-Zapero, J., Camacho, F., García-Santos, V., Verger, A., Lacaze, R., Weiss, M., Baret, F., Smets, B., 2020. Quality assessment of PROBA-V LAI, FAPAR and fCover collection 300 m products of Copernicus global land service. *Remote Sens.* 12, 1017. <https://doi.org/10.3390/rs12061017>.
- Garrigues, S., Lacaze, R., Baret, F., Morisette, J.T., Weiss, M., Nickeson, J.E., Fernandes, R., Plummer, S., Shabavan, N.V., Myneni, R.B., Knyazikhin, Y., Yang, W., 2008. Validation and intercomparison of global Leaf Area Index products derived from remote sensing data. *J. Geophys. Res. Biogeosci.* 113 <https://doi.org/10.1029/2007JG000635> n/a-n/a.
- Gastellu-Etchegorry, J.P., 2008. 3D modeling of satellite spectral images, radiation budget and energy budget of urban landscapes. *Meteorol. Atmos. Phys.* 102, 187–207. <https://doi.org/10.1007/s00703-008-0344-1>.
- Gough, C.M., Hardiman, B.S., Nave, L.E., Bohrer, G., Maurer, K.D., Vogel, C.S., Nadelhoffer, K.J., Curtis, P.S., 2013. Sustained carbon uptake and storage following moderate disturbance in a Great Lakes forest. *Ecol. Appl.* 23, 1202–1215. <https://doi.org/10.1890/12-1554.1>.
- Govaerts, Y., Verstraete, M.M., 1995. Modeling the scattering of light in three-dimensional canopies: contribution of a Monte Carlo ray tracing approach. In: *Combined Optical-Microwave Earth and Atmosphere Sensing - Conference Proceedings*, pp. 31–34.
- Govaerts, Y.M., Verstraete, M.M., 1998. Raytran: a Monte Carlo ray-tracing model to compute light scattering in three-dimensional heterogeneous media. *IEEE Trans. Geosci. Remote Sens.* 36, 493–505. <https://doi.org/10.1109/36.662732>.
- Grossmann, K., Frankenberg, C., Magney, T.S., Hurlock, S.C., Seibt, U., Stutz, J., 2018. PhotoSpec: a new instrument to measure spatially distributed red and far-red Solar-induced Chlorophyll Fluorescence. *Remote Sens. Environ.* 216, 311–327. <https://doi.org/10.1016/j.rse.2018.07.002>.
- Guanter, L., Zhang, Y., Jung, M., Joiner, J., Voigt, M., Berry, J.A., Frankenberg, C., Huete, A.R., Zarco-Tejada, P., Lee, J.E., Moran, M.S., Ponce-Campos, G., Beer, C., Camps-Valls, G., Buchmann, N., Gianelle, D., Klumpp, K., Cescatti, A., Baker, J.M., Griffis, T.J., 2014. Global and time-resolved monitoring of crop photosynthesis with chlorophyll fluorescence. *Proc. Natl. Acad. Sci. U. S. A.* 111, E1327–E1333. <https://doi.org/10.1073/pnas.1320008111>.
- He, L., Chen, J.M., Pisek, J., Schaaf, C.B., Strahler, A.H., 2012. Global clumping index map derived from the MODIS BRDF product. *Remote Sens. Environ.* 119, 118–130.
- He, L., Liu, J., Chen, J.M., Croft, H., Wang, R., Sprintsin, M., Zheng, T., Ryu, Y., Pisek, J., Gonsamo, A., Deng, F., Zhang, Y., 2016. Inter- and intra-annual variations of clumping index derived from the MODIS BRDF product. *Int. J. Appl. Earth Obs. Geoinf.* 44, 53–60. <https://doi.org/10.1016/j.jag.2015.07.007>.
- He, L., Chen, J.M., Liu, J., Mo, G., Joiner, J., 2017. Angular normalization of GOME-2 Sun-induced chlorophyll fluorescence observation as a better proxy of vegetation productivity. *Geophys. Res. Lett.* 44, 5691–5699. <https://doi.org/10.1002/2017GL073708>.
- Hogan, R.J., Quaife, T., Braghieri, R., 2018. Fast matrix treatment of 3-D radiative transfer in vegetation canopies: SPARTACUS-vegetation 1.1. *Geosci. Model Dev.* 11, 339–350. <https://doi.org/10.5194/gmd-11-339-2018>.
- Huang, D., Knyazikhin, Y., Dickinson, R.E., Rautiainen, M., Stenberg, P., Disney, M., Lewis, P., Cescatti, A., Tian, Y., Verhoef, W., Martonchik, J.V., Myneni, R.B., 2007. Canopy spectral invariants for remote sensing and model applications. *Remote Sens. Environ.* 106, 106–122.
- Jacquemoud, S., Baret, F., 1990. PROSPECT: a model of leaf optical properties spectra. *Remote Sens. Environ.* 34, 75–91. [https://doi.org/10.1016/0034-4257\(90\)90100-Z](https://doi.org/10.1016/0034-4257(90)90100-Z).
- Jacquemoud, S., Verhoef, W., Baret, F., Bacour, C., Zarco-Tejada, P.J., Asner, G.P., François, C., Ustin, S.L., 2009. PROSPECT+SAIL models: a review of use for vegetation characterization. *Remote Sens. Environ.* 113, S56–S66. <https://doi.org/10.1016/j.rse.2008.01.026>.
- Knyazikhin, Y., Schull, M.A., Stenberg, P., Mottus, M., Rautiainen, M., Yang, Y., Marshak, A., Latorre Carmona, P., Kaufmann, R.K., Lewis, P., Disney, M.J., Vanderbilt, V., Davis, A.B., Baret, F., Jacquemoud, S., Lyapustin, A., Myneni, R.B., 2013. Hyperspectral remote sensing of foliar nitrogen content. *Proc. Natl. Acad. Sci.* 110, E185–E192. <https://doi.org/10.1073/pnas.1210196109>.
- Kobayashi, H., Baldocchi, D.D., Ryu, Y., Chen, Q., Ma, S., Osuna, J.L., Ustin, S.L., 2012. Modeling energy and carbon fluxes in a heterogeneous oak woodland: a three-dimensional approach. *Agric. For. Meteorol.* 152, 83–100.
- Köhler, P., Frankenberg, C., Magney, T.S., Guanter, L., Joiner, J., Landgraf, J., 2018. Global retrievals of solar-induced chlorophyll fluorescence with TROPOMI: first results and intersensor comparison to OCO-2. *Geophys. Res. Lett.* 45, 10,456–10,463. <https://doi.org/10.1029/2018GL079031>.
- Kucharik, C.J., Norman, J.M., Gower, S.T., 1999. Characterization of radiation regimes in nonrandom forest canopies: theory, measurements, and a simplified modeling approach. *Tree Physiol.* 19, 695–706.
- Law, B.E., Cescatti, A., Baldocchi, D.D., 2001. Leaf area distribution and radiative transfer in open-canopy forests: implications for mass and energy exchange. *Tree Physiol.* <https://doi.org/10.1093/treephys/21.12.13.777>.
- Leblanc, S., Chen, J., Kwong, M., 2002. Tracing radiation and architecture of canopies. In: *TRAC Manual. Version 2.1. 3. Nat. Resour. Canada, Canada Cent.*, pp. 1–25.
- Leblanc, S.G., Chen, J.M., Fernandes, R., Deering, D.W., Conley, A., 2005. Methodology comparison for canopy structure parameters extraction from digital hemispherical photography in boreal forests. *Agric. For. Meteorol.* 129, 187–207.
- Lee, J.-E., Berry, J.A., van der Tol, C., Yang, X., Guanter, L., Damm, A., Baker, I., Frankenberg, C., 2015. Simulations of chlorophyll fluorescence incorporated into the Community Land Model version 4. *Glob. Chang. Biol.* 21, 3469–3477. <https://doi.org/10.1111/gcb.12948>.
- Li, Z., Zhang, Q., Li, J., Yang, X., Wu, Y., Zhang, Z., Wang, S., Wang, H., Zhang, Y., 2020. Solar-induced chlorophyll fluorescence and its link to canopy photosynthesis in maize from continuous ground measurements. *Remote Sens. Environ.* 236, 111420. <https://doi.org/10.1016/j.rse.2019.111420>.
- Liu, L., Liu, X., Wang, Z., Zhang, B., 2016. Measurement and analysis of bidirectional SIF emissions in wheat canopies. *IEEE Trans. Geosci. Remote Sens.* 54, 2640–2651. <https://doi.org/10.1109/TGRS.2015.2504089>.
- Loew, A., Van Bodegom, P.M., Widlowski, J.L., Otto, J., Quaife, T., Pinty, B., Raddatz, T., 2014. Do we (need to) care about canopy radiation schemes in DGVMs? Caveats and potential impacts. *Biogeosciences* 11, 1873–1897.
- Magney, T.S., Frankenberg, C., Fisher, J.B., Sun, Y., North, G.B., Davis, T.S., Kornfeld, A., Siebke, K., 2017. Connecting active to passive fluorescence with photosynthesis: a method for evaluating remote sensing measurements of Chl fluorescence. *New Phytol.* 215, 1594–1608. <https://doi.org/10.1111/nph.14662>.
- Magney, T.S., Bowling, D.R., Logan, B.A., Grossmann, K., Stutz, J., Blanken, P.D., Burns, S.P., Cheng, R., Garcia, M.A., Köhler, P., Lopez, S., Parazoo, N.C., Raczk, B., Schimel, D., Frankenberg, C., 2019. Mechanistic evidence for tracking the seasonality of photosynthesis with solar-induced fluorescence. *Proc. Natl. Acad. Sci. U. S. A.* 116, 11640–11645. <https://doi.org/10.1073/pnas.1900278116>.
- Magney, T.S., Barnes, M.L., Yang, X., 2020. On the covariation of chlorophyll fluorescence and photosynthesis across scales. *Geophys. Res. Lett.* 47 <https://doi.org/10.1029/2020gl091098>.
- Majasalmi, T., Bright, R.M., 2019. Evaluation of leaf-level optical properties employed in land surface models. *Geosci. Model Dev.* 12, 3923–3938. <https://doi.org/10.5194/gmd-12-3923-2019>.
- Malenovský, Z., Martin, E., Homolová, L., Gastellu-Etchegorry, J.P., Zurita-Milla, R., Schaeffer, M.E., Pokorný, R., Clevers, J.G.P.W., Cudlín, P., 2008. Influence of woody elements of a Norway spruce canopy on nadir reflectance simulated by the DART model at very high spatial resolution. *Remote Sens. Environ.* 112, 1–18.
- Meacham-Hensold, K., Montes, C.M., Wu, J., Guan, K., Fu, P., Ainsworth, E.A., Pederson, T., Moore, C.E., Brown, K.L., Raines, C., Bernacchi, C.J., 2019. High-throughput field phenotyping using hyperspectral reflectance and partial least squares regression (PLSR) reveals genetic modifications to photosynthetic capacity. *Remote Sens. Environ.* 231, 111176. <https://doi.org/10.1016/j.rse.2019.04.029>.
- Miao, G., Guan, K., Yang, X., Bernacchi, C.J., Berry, J.A., DeLucia, E.H., Wu, J., Moore, C. E., Meacham, K., Cai, Y., Peng, B., Kimm, H., Masters, M.D., 2018. Sun-induced chlorophyll fluorescence, photosynthesis, and light use efficiency of a soybean field from seasonally continuous measurements. *J. Geophys. Res. Biogeosci.* 123, 610–623. <https://doi.org/10.1002/2017JG004180>.
- Migliavacca, M., Perez-Priego, O., Rossini, M., El-Madany, T.S., Moreno, G., van der Tol, C., Rascher, U., Berninger, A., Bessenbacher, V., Burkart, A., Carrara, A., Fava, F., Guan, J.-H., Hammer, T.W., Henkel, K., Juarez-Alcalde, E., Julitta, T., Kolle, O., Martín, M.P., Musavi, T., Pacheco-Labrador, J., Pérez-Burgueno, A., Wutzler, T., Zaehle, S., Reichstein, M., 2017. Plant functional traits and canopy structure control the relationship between photosynthetic CO<sub>2</sub> uptake and far-red

- sun-induced fluorescence in a Mediterranean grassland under different nutrient availability. *New Phytol.* 214, 1078–1091. <https://doi.org/10.1111/nph.14437>.
- Nightingale, J., Schaeppman-Strub, G., Nickeson, J., Focus Area Leads, L., 2011. Assessing Satellite-derived Land Product Quality For Earth System Science Applications: Overview of the CEOS LPV Sub-group.
- Nilson, T., 1971. A theoretical analysis of the frequency of gaps in plant stands. *Agric. Meteorol.* 8, 25–38. [https://doi.org/10.1016/0002-1571\(71\)90092-6](https://doi.org/10.1016/0002-1571(71)90092-6).
- Ni-Meister, W., Yang, W., Kiang, N.Y., 2010. A clumped-foliage canopy radiative transfer model for a global dynamic terrestrial ecosystem model. I: theory. *Agric. For. Meteorol.* 150, 881–894. <https://doi.org/10.1016/j.agrformet.2010.02.009>.
- Norman, J.M., Jarvis, P.G., 1974. Photosynthesis in Sitka spruce (*Picea sitchensis* (Bong.) Carr.). III. Measurements of canopy structure and interception of radiation. *J. Appl. Ecol.* <https://doi.org/10.2307/240208>.
- Norman, J., Welles, J., 1983. Radiative transfer in an array of canopies. *Agron. J.* 75, 481–488.
- North, P.R., 1996. Three-dimensional forest light interaction model using a Monte Carlo method. *Geosci. Remote Sens. IEEE Trans.* 34, 946–956. <https://doi.org/10.1109/36.508411>.
- Norton, A.J., Rayner, P.J., Koffi, E.N., Scholze, M., Silver, J.D., Wang, Y.-P., 2019. Estimating global gross primary productivity using chlorophyll fluorescence and a data assimilation system with the BETHY-SCOPE model. *Biogeosciences* 16, 3069–3093. <https://doi.org/10.5194/bg-16-3069-2019>.
- Parazoo, N.C., Frankenberg, C., Köhler, P., Joiner, J., Yoshida, Y., Magney, T., Sun, Y., Yadav, V., 2019. Towards a harmonized long-term spaceborne record of far-red solar-induced fluorescence. *J. Geophys. Res. Biogeosci.* 124, 2518–2539. <https://doi.org/10.1029/2019JG005289>.
- Parazoo, N.C., Magney, T., Norton, A., Raczka, B., Bacour, C., Maignan, F., Baker, I., Zhang, Y., Qiu, B., Shi, M., Macbean, N., Bowling, D.R., Burns, S.P., Blanck, P.D., Stutz, J., Grossmann, K., Frankenberg, C., 2020. Wide discrepancies in the magnitude and direction of modeled solar-induced chlorophyll fluorescence in response to light conditions. *Biogeosciences* 17, 3733–3755. <https://doi.org/10.5194/bg-17-3733-2020>.
- Pinty, B., 2004. Radiation Transfer Model Intercomparison (RAMI) exercise: results from the second phase. *J. Geophys. Res.* 109, D06210 <https://doi.org/10.1029/2003JD004252>.
- Pinty, B., Gobron, N., Widlowski, J., Gerstl, S.A.W., Verstraete, M.M., Antunes, M., Bacour, C., Gascon, F., Gastellu, J.-P., Goel, N., Jacquemoud, S., North, P., Qin, W., Thompson, R., 2001. Radiation transfer model intercomparison (RAMI) exercise. *J. Geophys. Res. Atmos.* 106, 11937–11956. <https://doi.org/10.1029/2000JD900493>.
- Pinty, B., Lavergne, T., Dickinson, R.E., Widlowski, J.L., Gobron, N., Verstraete, M.M., 2006. Simplifying the interaction of land surfaces with radiation for relating remote sensing products to climate models. *J. Geophys. Res. Atmos.* 111.
- Pisek, J., Chen, J.M., Lacaze, R., Sonnentag, O., Alikas, K., 2010. Expanding global mapping of the foliage clumping index with multi-angular POLDER three measurements: evaluation and topographic compensation. *ISPRS J. Photogramm. Remote Sens.* 65, 341–346. <https://doi.org/10.1016/j.isprsjprs.2010.03.002>.
- Pisek, J., Ryu, Y., Sprintsin, M., He, L., Oliphant, A.J., Korhonen, L., Kuusk, J., Kuusk, A., Bergstrom, R., Verrelst, J., Alikas, K., 2013. Retrieving vegetation clumping index from Multi-angle Imaging SpectroRadiometer (MISR) data at 275nm resolution. *Remote Sens. Environ.* 138, 126–133. <https://doi.org/10.1016/j.rse.2013.07.014>.
- Pisek, J., Govind, A., Arndt, S.K., Hocking, D., Wardlaw, T.J., Fang, H., Matteucci, G., Longdoz, B., 2015a. Intercomparison of clumping index estimates from POLDER, MODIS, and MISR satellite data over reference sites. *ISPRS J. Photogramm. Remote Sens.* 101, 47–56. <https://doi.org/10.1016/j.isprsjprs.2014.11.004>.
- Pisek, J., Govind, A., Arndt, S.K., Hocking, D., Wardlaw, T.J., Fang, H., Matteucci, G., Longdoz, B., 2015b. Intercomparison of clumping index estimates from POLDER, MODIS, and MISR satellite data over reference sites. *ISPRS J. Photogramm. Remote Sens.* 101, 47–56. <https://doi.org/10.1016/j.isprsjprs.2014.11.004>.
- Prentice, I.C., Liang, X., Medlyn, B.E., Wang, Y.-P., 2015. Reliable, robust and realistic: the three R's of next-generation land-surface modelling. *Atmos. Chem. Phys.* 15, 5987–6005. <https://doi.org/10.5194/acp-15-5987-2015>.
- Qiu, B., Chen, J.M., Ju, W., Zhang, Q., Zhang, Y., 2019. Simulating emission and scattering of solar-induced chlorophyll fluorescence at far-red band in global vegetation with different canopy structures. *Remote Sens. Environ.* 233, 111373. <https://doi.org/10.1016/j.rse.2019.111373>.
- Ross, J., 1981. The Radiation Regime and Architecture of Plant Stands. Junk, Boston. <https://doi.org/10.1007/978-94-009-8647-3>.
- Ryu, Y., Nilson, T., Kobayashi, H., Sonnentag, O., Law, B.E., Baldocchi, D.D., 2010a. On the correct estimation of effective leaf area index: does it reveal information on clumping effects? *Agric. For. Meteorol.* 150, 463–472.
- Ryu, Y., Sonnentag, O., Nilson, T., Vargas, R., Kobayashi, H., Wenk, R., Baldocchi, D.D., 2010b. How to quantify tree leaf area index in an open savanna ecosystem: a multi-instrument and multi-model approach. *Agric. For. Meteorol.* 150, 63–76. <https://doi.org/10.1016/j.agrformet.2009.08.007>.
- Ryu, Y., Berry, J.A., Baldocchi, D.D., 2019. What is global photosynthesis? History, uncertainties and opportunities. *Remote Sens. Environ.* 223, 95–114. <https://doi.org/10.1016/j.rse.2019.01.016>.
- Schimel, D., Schneider, F.D., 2019. Flux towers in the sky: global ecology from space. *New Phytol.* 224, 570–584. <https://doi.org/10.1111/nph.15934>.
- Schimel, D., Stephens, B.B., Fisher, J.B., 2015. Effect of increasing CO<sub>2</sub> on the terrestrial carbon cycle. *Proc. Natl. Acad. Sci.* 112, 436–441. <https://doi.org/10.1073/pnas.1407302112>.
- Schmid, H.P., 2003. Ecosystem-atmosphere exchange of carbon dioxide over a mixed hardwood forest in northern lower Michigan. *J. Geophys. Res.* 108, 4417. <https://doi.org/10.1029/2002JD003011>.
- Schwarz, G., 1978. Estimating the dimension of a model. *Ann. Stat.* 6, 461–464.
- Sellers, P.J., 1985. Canopy reflectance, photosynthesis and transpiration. *Int. J. Remote Sens.* 6, 1335–1372. <https://doi.org/10.1080/01431168508948283>.
- Sellers, P.J., 1997. Modeling the exchanges of energy, water, and carbon between continents and the atmosphere. *Science* (80-. ) 275, 502–509. <https://doi.org/10.1126/science.275.5299.502>.
- Serbin, S.P., Singh, A., McNeil, B.E., Kingdon, C.C., Townsend, P.A., 2014. Spectroscopic determination of leaf morphological and biochemical traits for northern temperate and boreal tree species. *Ecol. Appl.* 24, 1651–1669. <https://doi.org/10.1890/13-2110.1>.
- Singh, A., Serbin, S.P., McNeil, B.E., Kingdon, C.C., Townsend, P.A., 2015. Imaging spectroscopy algorithms for mapping canopy foliar chemical and morphological traits and their uncertainties. *Ecol. Appl.* 25, 2180–2197. <https://doi.org/10.1890/14-2098.1>.
- Sinoquet, H., Le Roux, X., Adam, B., Ameglio, T., Daudet, F.A., 2001. RATP: a model for simulating the spatial distribution of radiation absorption, transpiration and photosynthesis within canopies: application to an isolated tree crown. *Plant Cell Environ.* 24, 395–406. <https://doi.org/10.1046/j.1365-3040.2001.00694.x>.
- Smolander, S., Stenberg, P., 2005. Simple parameterizations of the radiation budget of uniform broadleaved and coniferous canopies. *Remote Sens. Environ.* 94, 355–363.
- Song, C., Katul, G., Oren, R., Band, L.E., Tague, C.L., Stoy, P.C., McCarthy, H.R., 2009. Energy, water, and carbon fluxes in a loblolly pine stand: results from uniform and gappy canopy models with comparisons to eddy flux data. *J. Geophys. Res. Biogeosci.* 114, 1–18. <https://doi.org/10.1029/2009JG000951>.
- Sprintsin, M., Chen, J.M., Desai, A., Gough, C.M., 2012. Evaluation of leaf-to-canopy upscaling methodologies against carbon flux data in North America. *J. Geophys. Res. Biogeosci.* 117 <https://doi.org/10.1029/2010JG001407>.
- Taylor, T.E., Eldering, A., Merrelli, A., Kiel, M., Somkuti, P., Cheng, C., Rosenberg, R., Fisher, B., Crisp, D., Basilio, R., Bennett, M., Cervantes, D., Chang, A., Dang, L., Frankenberg, C., Haemmerle, V.R., Keller, G.R., Kurosu, T., Laughner, J.L., Lee, R., Marchetti, Y., Nelson, R.R., O'Dell, C.W., Osterman, G., Pavlick, R., Roehl, C., Schneider, R., Spiers, G., To, C., Wells, C., Wennberg, P.O., Yelamanchili, A., Yu, S., 2020. OCO-3 early mission operations and initial (vEarly) XCO<sub>2</sub> and SIF retrievals. *Remote Sens. Environ.* 251, 112032. <https://doi.org/10.1016/j.rse.2020.112032>.
- Tournebize, R., Sinoquet, H., 1995. Light interception and partitioning in a shrub/grass mixture. *Agric. For. Meteorol.* 72, 277–294.
- Tucker, C.J., 1979. Red and photographic infrared linear combinations for monitoring vegetation. *Remote Sens. Environ.* 8, 127–150. [https://doi.org/10.1016/0034-4257\(79\)90013-0](https://doi.org/10.1016/0034-4257(79)90013-0).
- van der Tol, C., Verhoef, W., Timmermans, J., Verhoef, A., Su, Z., 2009. An integrated model of soil-canopy spectral radiances, photosynthesis, fluorescence, temperature and energy balance. *Biogeosciences* 6, 3109–3129. <https://doi.org/10.5194/bg-6-3109-2009>.
- Van Der Tol, C., Berry, J.A., Campbell, P.K.E., Rascher, U., 2014. Models of fluorescence and photosynthesis for interpreting measurements of solar-induced chlorophyll fluorescence. *J. Geophys. Res. Biogeosci.* 119, 2312–2327. <https://doi.org/10.1002/2014JG002713>.
- van der Tol, C., Rossini, M., Cogliati, S., Verhoef, W., Colombo, R., Rascher, U., Mohammed, G., 2016. A model and measurement comparison of diurnal cycles of sun-induced chlorophyll fluorescence of crops. *Remote Sens. Environ.* 186, 663–677. <https://doi.org/10.1016/j.rse.2016.09.021>.
- Verger, A., Baret, F., Weiss, M., 2019. Algorithm Theoretical Basis Document - Leaf Area Index (LAI) - Collection 1km - Version 2.
- Verhoef, W., 1984. Light scattering by leaf layers with application to canopy reflectance modeling: the SAIL model. *Remote Sens. Environ.* [https://doi.org/10.1016/0034-4257\(84\)90057-9](https://doi.org/10.1016/0034-4257(84)90057-9).
- Vilfan, N., van der Tol, C., Müller, O., Rascher, U., Verhoef, W., 2016. Fluspect-B: a model for leaf fluorescence, reflectance and transmittance spectra. *Remote Sens. Environ.* 186, 596–615. <https://doi.org/10.1016/j.rse.2016.09.017>.
- Wang, Y.P., Jarvis, P.G., 1990a. Description and validation of an array model — MAESTRO. *Agric. For. Meteorol.* 51, 257–280. [https://doi.org/10.1016/0168-1923\(90\)90112-J](https://doi.org/10.1016/0168-1923(90)90112-J).
- Wang, Y.P., Jarvis, P.G., 1990b. Influence of crown structural properties on PAR absorption, photosynthesis, and transpiration in Sitka spruce: application of a model (MAESTRO). *Tree Physiol.* 7, 297–316. <https://doi.org/10.1093/treephys/7.1-2-3-4.297>.
- Wang, K., Kumar, P., 2019. Characterizing relative degrees of clumping structure in vegetation canopy using waveform LiDAR. *Remote Sens. Environ.* 232, 111281. <https://doi.org/10.1016/j.rse.2019.111281>.
- Widlowski, J.L., Taberner, M., Pinty, B., Bruniquel-Pinel, V., Disney, M., Fernandes, R., Gastellu-Etchegorry, J.P., Gobron, N., Kuusk, A., Lavergne, T., Leblanc, S., Lewis, P. E., Martin, E., Möttus, M., North, P.R.J., Qin, W., Robustelli, M., Rochdi, N., Ruiloba, R., Soler, C., Thompson, R., Verhoef, W., Verstraete, M.M., Xie, D., 2007. Third Radiation Transfer Model Intercomparison (RAMI) exercise: documenting progress in canopy reflectance models. *J. Geophys. Res. Atmos.* 112, 1–28. <https://doi.org/10.1029/2006JD007821>.
- Widlowski, J.L., Pinty, B., Clerici, M., Dai, Y., De Kauwe, M., De Ridder, K., Kallel, A., Kobayashi, H., Lavergne, T., Ni-Meister, W., Olchev, A., Quaife, T., Wang, S., Yang, W., Yang, Y., Yuan, H., 2011. RAMI4PILPS: an intercomparison of formulations for the partitioning of solar radiation in land surface models. *J. Geophys. Res. G Biogeosci.* 116.
- Widlowski, J.L., Pinty, B., Lopatka, M., Atzberger, C., Buzica, D., Chelle, M., Disney, M., Gastellu-Etchegorry, J.P., Gerboles, M., Gobron, N., Grau, E., Huang, H., Kallel, A., Kobayashi, H., Lewis, P.E., Qin, W., Schlerf, M., Stuckens, J., Xie, D., 2013. The fourth radiation transfer model intercomparison (RAMI-IV): proficiency testing of

- canopy reflectance models with ISO-13528. *J. Geophys. Res. D Atmos.* 118, 6869–6890.
- Widlowski, J.L., Mio, C., Disney, M., Adams, J., Andredakis, I., Atzberger, C., Brennan, J., Busetto, L., Chelle, M., Ceccherini, G., Colombo, R., Côté, J.F., Eenmäe, A., Essery, R., Gastellu-Etchegorry, J.P., Gobron, N., Grau, E., Haverd, V., Homolová, L., Huang, H., Hunt, L., Kobayashi, H., Koetz, B., Kuusk, A., Kuusk, J., Lang, M., Lewis, P.E., Lovell, J.L., Malenovský, Z., Meroni, M., Morsdorf, F., Möttus, M., Ni-Meister, W., Pinty, B., Rautiainen, M., Schlerf, M., Somers, B., Stuckens, J., Verstraete, M.M., Yang, W., Zhao, F., Zenone, T., 2015. The fourth phase of the radiative transfer model intercomparison (RAMI) exercise: actual canopy scenarios and conformity testing. *Remote Sens. Environ.* 169, 418–437. <https://doi.org/10.1016/j.rse.2015.08.016>.
- Wieder, W.R., Cleveland, C.C., Smith, W.K., Todd-Brown, K., 2015. Future productivity and carbon storage limited by terrestrial nutrient availability. *Nat. Geosci.* 8, 441–444. <https://doi.org/10.1038/ngeo2413>.
- Wieneke, S., Burkart, A., Cendrero-Mateo, M.P., Julitta, T., Rossini, M., Schickling, A., Schmidt, M., Rascher, U., 2018. Linking photosynthesis and sun-induced fluorescence at sub-daily to seasonal scales. *Remote Sens. Environ.* 219, 247–258. <https://doi.org/10.1016/j.rse.2018.10.019>.
- Yan, G., Hu, R., Luo, J., Weiss, M., Jiang, H., Mu, X., Xie, D., Zhang, W., 2019. Review of indirect optical measurements of leaf area index: recent advances, challenges, and perspectives. *Agric. For. Meteorol.* 265, 390–411. <https://doi.org/10.1016/j.agrformet.2018.11.033>.
- Yang, P., van der Tol, C., 2018. Linking canopy scattering of far-red sun-induced chlorophyll fluorescence with reflectance. *Remote Sens. Environ.* 209, 456–467. <https://doi.org/10.1016/j.rse.2018.02.029>.
- Yang, W., Ni-Meister, W., Kiang, N.Y., Moorcroft, P.R., Strahler, A.H., Oliphant, A., 2010. A clumped-foliage canopy radiative transfer model for a Global Dynamic Terrestrial Ecosystem Model II: comparison to measurements. *Agric. For. Meteorol.* 150, 895–907. <https://doi.org/10.1016/j.agrformet.2010.02.008>.
- Yang, X., Tang, J., Mustard, J.F., Lee, J.-E., Rossini, M., Joiner, J., Munger, J.W., Kornfeld, A., Richardson, A.D., 2015. Solar-induced chlorophyll fluorescence that correlates with canopy photosynthesis on diurnal and seasonal scales in a temperate deciduous forest. *Geophys. Res. Lett.* 42, 2977–2987. <https://doi.org/10.1002/2015GL063201>.
- Yang, P., Verhoef, W., van der Tol, C., 2017. The mSCOPE model: a simple adaptation to the SCOPE model to describe reflectance, fluorescence and photosynthesis of vertically heterogeneous canopies. *Remote Sens. Environ.* 201, 1–11. <https://doi.org/10.1016/j.rse.2017.08.029>.
- Yang, K., Ryu, Y., Dechant, B., Berry, J.A., Hwang, Y., Jiang, C., Kang, M., Kim, J., Kimm, H., Kornfeld, A., Yang, X., 2018. Sun-induced chlorophyll fluorescence is more strongly related to absorbed light than to photosynthesis at half-hourly resolution in a rice paddy. *Remote Sens. Environ.* 216, 658–673. <https://doi.org/10.1016/j.rse.2018.07.008>.
- Yang, P., van der Tol, C., Verhoef, W., Damm, A., Schickling, A., Kraska, T., Muller, O., Rascher, U., 2019. Using reflectance to explain vegetation biochemical and structural effects on sun-induced chlorophyll fluorescence. *Remote Sens. Environ.* 231, 0–1. <https://doi.org/10.1016/j.rse.2018.11.039>.
- Zeng, Y., Badgley, G., Dechant, B., Ryu, Y., Chen, M., Berry, J.A., 2019. A practical approach for estimating the escape ratio of near-infrared solar-induced chlorophyll fluorescence. *Remote Sens. Environ.* 232, 111209. <https://doi.org/10.1016/j.rse.2019.05.028>.